PRODEX-ESA-SSTC Contract No 170724

The Charged Particle Detector (CPD): Electron and Proton spectra

Technical Note B

Mathias Cyamukungu ***Peter Stauning***
Ghislain Grégoire ***Joseph Lemaire***

Space Radiation Group
Université Catholique de Louvain-la-Neuve

Danish Meteorological Institute

Belgian Institute for Space Aeronomy

January 2001

Contents

Preface

Large flares at the sun and magnetic storms and substorms in the Earth's magnetosphere may generate intense radiation of high-energy charged particles, mostly electrons, protons and α-particles, which add to the steady background of cosmic radiation. This high-energy radiation is an important element of the fundamental physical processes at the sun, in the interplanetary space and in the near-earth space. The high-energy particles are also important elements of substorm generation and dynamics and of importance for various aspects of upper atmosphere conditions. The high-energy charged particles of solar or magnetospheric origin may be temporarily trapped in the Earth's magnetic field until lost by precipitation into the atmosphere. The precipitation is particularly intense in the polar and auroral regions where the energetic radiation may produce substantially enhanced ionization at low altitudes. Such ionization can cause black-out of HF radio communication circuits used, among other, for the air and sea traffic. In addition, the high-energy particle precipitation increases the conductivity of the atmosphere thereby changing its global electrical properties. The precipitation may even produce modifications of the lower atmospheric chemistry and composition, for instance, the nitric- oxide and ozone abundance. The energetic particle radiation may have various adverse effects e.g. on space systems, on communications and on the environment. The high-energy radiation during large solar flares may cause severe damage on spacecraft systems in particular on solar panels and complex electronic systems. The high-energy charged particles are important in a number of research fields such as investigations of solar wind-magnetosphere boundary conditions and other essential geomagnetic morphological problems like the distinguishing between 'open' and 'closed' magnetospheric regions. The high-energy precipitation events may offer essential advantages for atmospheric observations. The ionization produced at low altitudes makes the upper atmosphere 'visible' for electromagnetic probing and thus enable various forms of radar observations of winds and turbulence in the 'middle atmosphere' which is difficult to explore by other methods. The solid-state high energy charged particle detector (CPD) experiment was proposed in 1991 for the Danish small satellite named ØRSTED. It is aiming at the detection of electrons in the energy range from 50 keV to $>$ 1 Mev and protons and α-particles from 300 keV to $>$ 30 MeV. The primary objectives for the satellite particle experiment are:

- *detection of the energetic particle radiation in the upper polar atmosphere to be combined with absorption data from imaging riometer installations on the ground in order to detect the atmospheric reactions and the dynamical features of polar and auroral particle precipitation events.*
- *investigation of the properties of the radiation trapped in the Earth's magnetic field and monitoring of the long-term high-energy particle radiation dose at the satellite for investigations of possible radiation damages on other on-board experiments and systems.*
- *monitoring of the level of solar-geophysical activity during events like major solar flares and geomagnetic storms where intense and variable high-energy particle radiation may occur.*

Useful addresses

Danish Meteorological Institute
Solar-Terrestrial Physics Division
Lyngbyvej 100,
DK-2100 Copenhagen, Denmark
FAX: 45 39 27 10 80 TEL: 45 39 15 75 00

Space Radiation Group
Université Catholique de Louvain
2, chemin du Cyclotron,
B-1348 Louvain-La-Neuve, Belgium
FAX: 32 10 45 2183 TEL: 32 10 47 3273

Belgian Institute for Space Aeronomy
3 avenue Circulaire, B-1180 Brussels, Belgium
FAX: 32 2 374 8423 TEL: 32 2 374 8121

ESA/ESTEC - PRODEX
P.O. Box 299
Keplerlaan 1, 2200 AG Noordwijk, The Netherlands
FAX: 31 71 565 4693 TEL: 31 71 565 4350

SSTC
Rue de la Science, 8
1000 Brussels, Belgium
FAX: 32 2 230 59 12 TEL: 32 2 238 34 11

Useful e-mail adresses and phone numbers

Torsten Neubert	*TEL: 45 39 15 75 00*	*neubert@dmi.min.dk*
Peter Stauning	*TEL: 45 39 15 74 73*	*pst@dmi.dk*
Mathias Cyamukungu	*TEL: 32 10 47 3402*	*cyam@fynu.ucl.ac.be*
Ghislain Grégoire	*TEL: 32 10 47 3216*	*gregoire@fynu.ucl.ac.be*
Joseph Lemaire	*TEL: 32 2 373 0407*	*joseph.lemaire@bira-iasb.oma.be*
Daniel Heynderickx	*TEL: 32 2 373 0417*	*daniel.heynderickx@bira-iasb.oma.be*
Michel Kruglanski	*TEL: 32 2 373 0417*	*michel.kruglanski@bira-iasb.oma.be*
H. Olthof (PRODEX)	*TEL: 31 71 565 46 93*	
J.W. Bernard (SSTC)	*TEL: 32 2 238 35 83*	
M.C. Limbourg (SSTC)	*TEL: 32 2 238 34 11*	

Acknowledgments

The data analysis phase of the CPD experiment made us very reliant to computing resources. We would like to thank Dr. A. Ninane, head of the computer staff at UCL/FYNU, for all the data storage space and the extra - CPU time he has unearthed to keep the extraction of proton and electron spectra running.

System engineer Peter Davidsen, formerly at DMI, now at Terma A/S, has provided invaluable assistance through all phases of the construction, testing and calibration of the CPD instrument, in its integration in the ØRSTED payload and in post-launch operation of the experiment.

Dr. D. Heynderickx and Dr. M. Kruglanski have shown much interest in this work and given useful comments on the final results.

Dr. M. Cyamukungu is grateful to the PRODEX-ESA-SSTC management team for the allowed contract extension following the delayed launch of the ØRSTED satellite. The results presented in this report are much worth the effort.

Of course, the authors endorse solely the responsibility for the contents of this report.

Introduction

The satellite
ØRSTED is the first mission in the Danish small satellite program. It has a total weight of 62 kg. The dimensions of the body is 34 x 45 x 72 cm and it holds a coilable boom of 8 m length to carry the The ØRSTED satellite was launched on February 23, 1999. Its orbit characteristics as of February 10, 2000 are listed below:

```
Launch:
-------
Vandenberg AFB on February 23, 1999, at 10:29:55 GMT

Initial conditions:
-------------------
apogee  865 km
perigee  649 km
argument of perigee  224 deg
ascending node  14:11 LT (drifting towards noon)
drift of orbit plane  0.76 deg/day

Orbit parameters as of February 10, 2000:
-----------------------------------------
inclination 96.48 deg
semi major axis  7128 km
eccentricity  0.015
anomalistic period  99.82 min
nodal period  99.99 min
perigee drift  -3.15 deg/day
longitude increment  -24.99 deg/orbit
```

The CPD experiment *The Charged Particle Detector (CPD) dedicated to measure the flux of charged particles along the satellite orbit was designed and calibrated by Dr. P. Stauning at the Danish Meteorological Institute (DMI). The instrument comprises an array of 6 solid-state silicon detector assemblies. The detectors are mounted in a box which also holds all electronic circuits involved in the experiment, that is, high-voltage supply for the detectors, charge- sensitive preamplifiers, pulse amplifiers, discriminators, counter circuits, and a computer system based on the intel 80186 processor circuits. The detector designations and locations are shown in Figure 1.*

Figure 2 presents a simplified block diagram of the electronic system. Each detector has its own

charge-sensitive pre-amplifier (CSA), pulse amplifier, 4- or 8-level pulse-height analyser (PHA) and buffer counter circuit. The individual pulses, when shaped by the CSA stage, have a width of 0.8 μsec. The counters are sampled by a microprocessor system, which also samples housekeeping voltage and temperature data. The microprocessor controls the operation of the instrument; it receives mode shift commands from, and it communicates data and status to the satellite main central data handling (CDH) computer. A calibration circuit also controlled by the microprocessor may inject calibration pulses at the front end of the CSA stage. The experiment has been electrically tested and calibrated in the laboratory at DMI and calibrated in proton and electron beams at the High-Energy Radiation Facility at NASA Goddard Space Flight Center.
A first numerical calibration of the instrument was performed at the University of Louvain by Dr. M. Cyamukungu and Pr. Gh. Grégoire [2]. Following a change of the shielding thickness in September 1998, it was necessary to perform a second numerical calibration from which the characteristics summarized in Table 1 resulted. Also, new efficiency values had to be calculated. They are presented in Chapter 2 and serve as the basis for electron and proton spectra extraction. This spectrum extraction method is described in Chapter 3 and applied in Chapter 4.

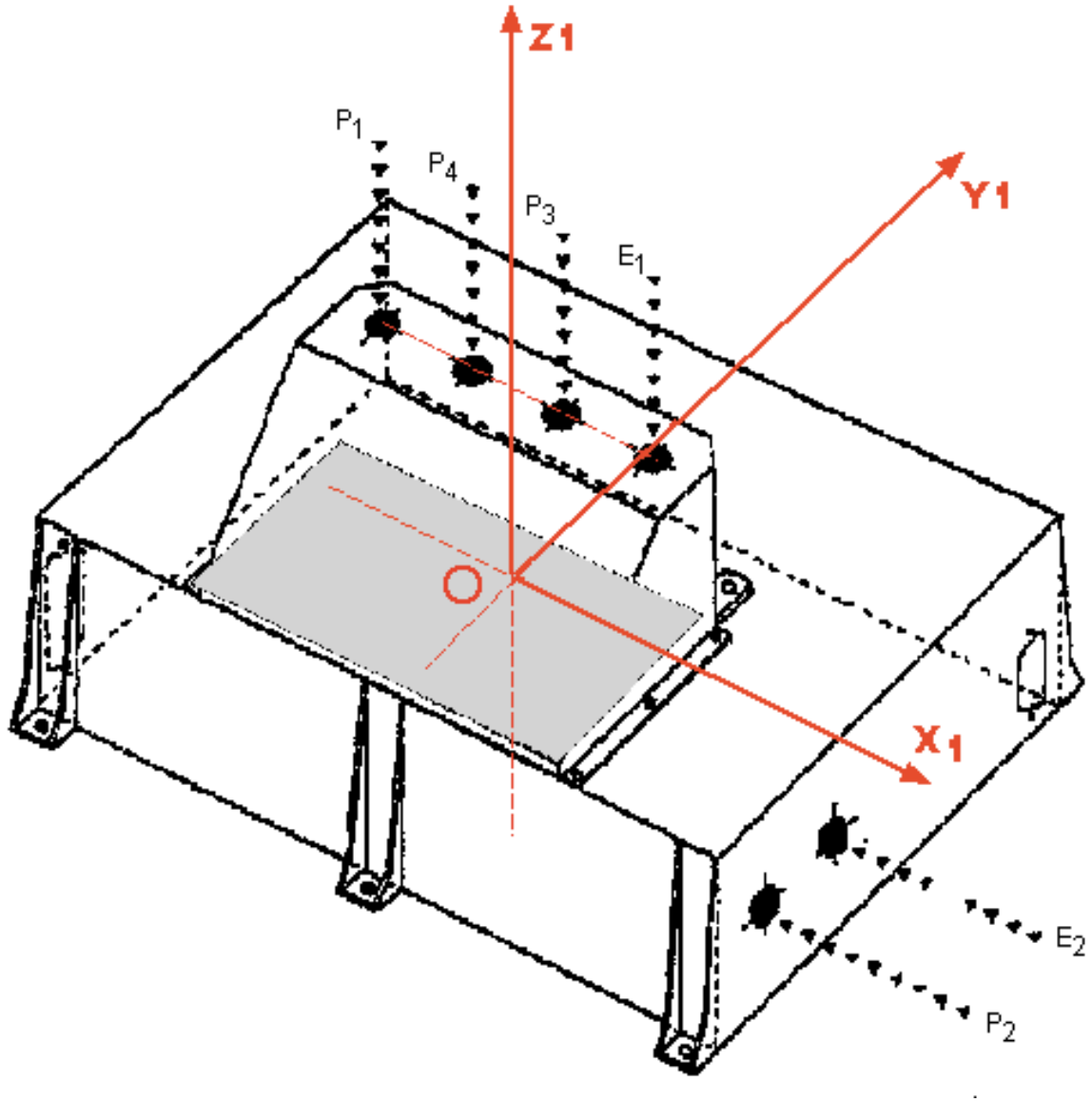

Figure 1: The CPD box and detector location. It is accomodated on the ØRSTED satellite such that the Z1 axis looks in the direction of the satellite magnetometer boom.

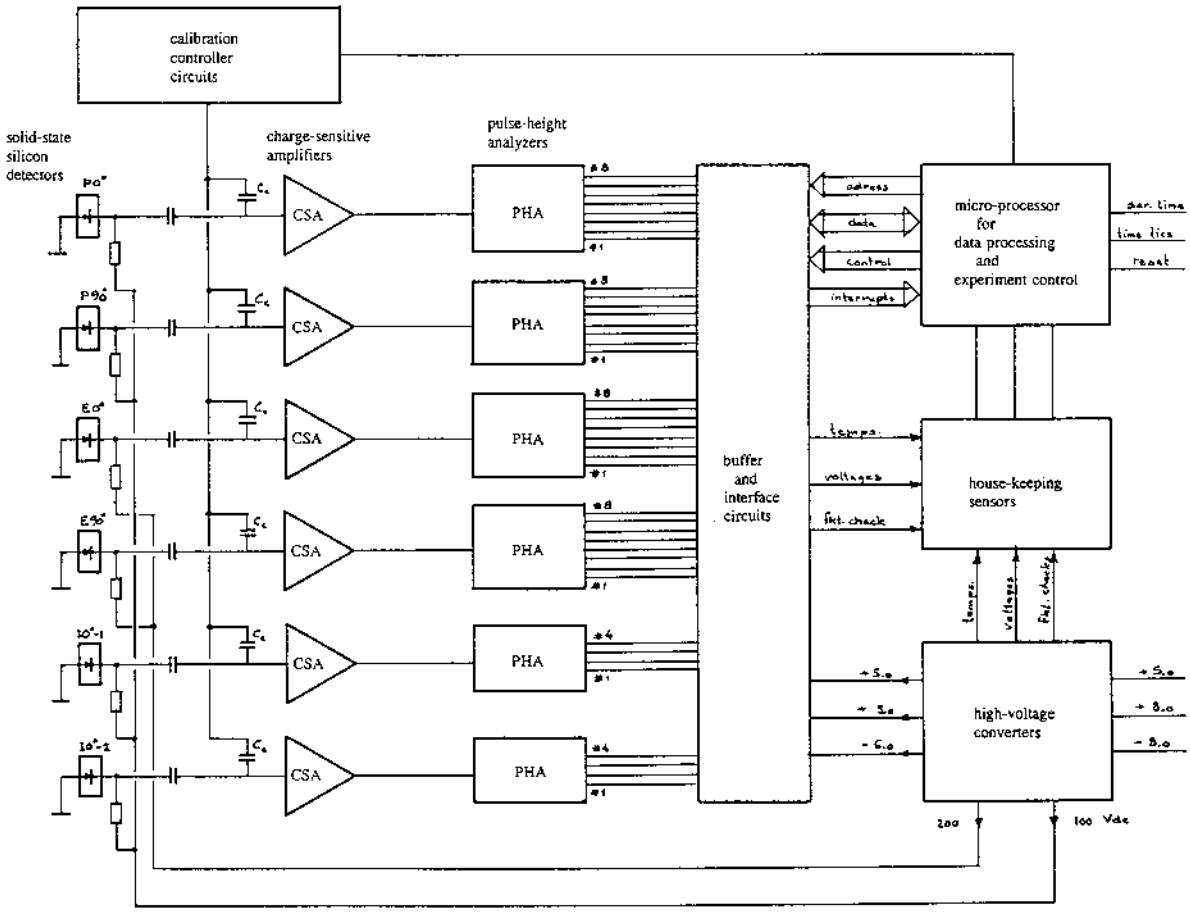

Figure 2: Simplified electrical block diagram of the CPD particle experiment.

Property	*DETECTOR*			
	P1 and P2	*P3*	*P4*	*E1 and E2*
Sight angle (degree)	*90 0*	*90*	*90*	*90 0*
F.O.V half angle (degree)	*20.5*	*33.5*	*33.5*	*20.5*
Aperture (cm^2)	*0.196*	*0.283*	*0.283*	*0.196*
Geometric factor ($cm^2\ sr$)	*0.053*	*0.25*	*0.25*	*0.053*
Entrance window ($\mu m/compound$)	*1.25/Ni*	*1000/Al*	*1000/Cu*	*1.25/Ni*
Detector type	*A*	*A*	*A*	*B*
THRESHOLD ENERGIES (MeV)				
α*:*	*.51*	*51.9*	*89.9*	*.51*
	.53	*52.0*	*90.1*	*.53*
	.71	*52.5*	*90.7*	*.71*
p*:*	*.23*	*12.9*	*22.3*	*.23*
	.24	*13.0*	*22.5*	*.24*
	.29	*13.2*	*22.8*	*.29*
e^-*:*	*.02*	*.68*	*1.75*	*.02*
	.02	*.78*	*2.2*	*.02*
	.07	*2.33*	*>6.*	*.067*
PEAK (PENETRATION) ENERGY:				
α	*24.*	*59.*	*95.*	*48.*
p	*6.*	*15.*	*24.*	*12.*
e^-	*.37*	*1.00*	*2.1*	*.88*
MEAN ENERGY LOST IN Si at PEAK (PENETRATION) ENERGY:				
α	*22.8*	*22.8*	*22.8*	*48.*
p	*5.6*	*5.6*	*5.6*	*12.*
e^-	*.3*	*.3*	*.3*	*.8*
ENERGY BIN LIMITS (keV):				
1	*423 417*	*209*	*212*	*47*
2	*639 629*	*741*	*752*	*72*
3	*989 974*	*2183*	*2146*	*111*
4	*1500 1478*	*7742*	*7611*	*168*
5	*2146 2146*			*237*
6	*3241 3241*			*358*
7	*5015 5015*			*553*
8	*7611 7611*			*840*

Table 1: Properties of the CPD array. ***A - type detector****: TU-011-050-300;* ***B - type detector****: TU-016-050-1000*

The first chapter of this report is devoted to a survey of the ØRSTED/CPD raw data.

Chapter 1

The ØRSTED/CPD raw data

1.1 The counting rates and time tags

The CPD data covering the time period from April to October 1999 were delivered on seven 650 Mbyte CD-ROM's. The CD-ROM data collected during each day (ddd) of the year (yy) and each hour (hh) are grouped into a file named "CPDyyddd.hh" . In general, the sampling rate is about 1/2 Hz, which corresponds to a distance resolution of about 15 km. Below is an excerpt from the file CPD99274.00.

```
year month day hour minute sec xxx xxx xxx livetime
99 10  1  0 27 30.658  25  34    851   2000
      71      67      64      57      50      29      17       9  P1
    2496    1920    1276     632     286     113      90      84  E1
      69      64      45       5                                   P4
      78      70      43       6                                   P3
    4064     322     189     130      88      51      28       6  P2
  234496  205312  156160   97792   46848    8608     844     205  E2
99 10  1  0 27 32.658  26  34    852   2000
      83      77      74      67      53      35      22      11
    2376    1796    1180     584     271     102      87      81
      70      62      39       9
      91      83      56      13
    4000     302     141      96      75      36      18       6
  233984  204288  155136   96768   46336    8448     836     205
99 10  1  0 27 34.658  27  34    853   2000
      74      68      68      63      59      40      27      17
    2488    1892    1204     624     286     116      95      90
      83      74      55      10
      90      83      51      11
    3952     326     157     101      72      40      19       8
  234496  204288  154112   96000   45568    8416     810     180
99 10  1  0 27 36.658  28  34    854   2000
      60      57      53      47      38      23      14       9
    2416    1820    1192     576     244      91      73      70
      63      59      38      13
      91      82      48      10
    3896     321     177     127      88      47      19       4
  233984  203776  153088   94976   45312    8256     786     179
```

Data files are made of successive 7-lines records: The first line contains among others, a time tag (year, month, day, hour, minute and seconds) and the data acquisition time (in milliseconds). The next six lines of a records are made of the counting rates drawn from each detector channel. The detector names are listed as P1 to E2 in the record margin. The channel numbers are listed in an increasing order from channel number 1 to channel number 8 (for detectors P1, E1, P2 and E2) or to channel 4 (for detectors P3 and P4).
At first glance and by use of the detection efficiencies of each channel available in [4] or in Chapter 2 of this report, one can draw some preliminary characteristics of the electron and proton spectra:

- *The up-looking detector E1 counts about two orders of magnitude less than its side-looking equivalent E2. This rather high anisotropic effect is found also for channel 1 of the up-looking P1 and its side-looking equivalent P2. The detection efficiency curves show that the high anisotropy is common and almost limited to channels with significant detection efficiency for electrons.*
- *The P3 detector is shielded by a 1 mm thick aluminum plate and the P4 detector is shielded by a 1 mm copper plate. The consequence of such shielding setup may be seen in the efficiency function: one expects that the P3 detector will have a higher counting rate than P4 in all their channels having the same number. This was in general observed (and at times used to ascribe the right detector to the right line in the data file), but some records display P4 counts that are higher than P3 ones for all or part of the channels. A very few records were detected where this P4 higher counts falls out of the limit determined on the assumption of poissonnian statistical distribution of counts. Further investigations are needed to evaluate the relative number of such events and decide weither they deserve a carefull analysis or not.*

The acquisition time for each record appears to be likened to the usual livetime. No dead-time was measured by the CPD and the results presented in the following chapters are valid only under the assumption that the whole CPD has been able to handle (without significant dead-time) counting rates as high as the $\sim 10^5\ counts/sec$ observed in the first channel of E2.

1.2 The ØRSTED ephemeris file

An excerpt of the ephemeris file downloaded from the ØRSTED data center follows. It contains, among others, the satellite positions in cartesian GEO coordinates and the corresponding time tags (http://web.dmi.dk/projects/oersted/SDC/oersted.html).

```
ØRSTED Almanac File.
Contents: Position and velocity in cartesian ECEF coordinates and position
in local, geodedic coordinates. Geomagnetic coordinates and local time,
and magnetic footprints (direct and conjugate) based on AACGM.
Satellite attitude wrt. orbit plane.
Units are: km, km/s, degrees and nT as appropriate.
Revision.
  Time (UTC)       x         y         z         vx        vy        vz       alt      lat      lon     mlat  ...
19990331 00:00  6127.560  3407.984   671.552  1.355571 -0.812872 -7.482946  665.660   5.5077   29.0816 -18.17 ...
19990331 00:05  6209.777  2991.829 -1569.362 -0.816251 -1.919980 -7.328936  692.241 -12.9099   25.7245 -27.98 ...
19990331 00:10  5644.527  2286.053 -3652.230 -2.921423 -2.728121 -6.441783  728.633 -31.1220   22.0481 -42.31 ...
19990331 00:15  4486.097  1391.844 -5372.006 -4.736263 -3.169111 -4.932283  769.886 -49.0256   17.2369 -52.92 ...
19990331 00:20  2850.296   423.204 -6566.022 -6.077730 -3.225475 -2.968080  810.300 -66.4467    8.4454 -62.20 ...
```

The satellite position is provided in the standard almanac files (available on web) at a rate of 1/300 Hz, but has been made available at 1/60 Hz. Initially, the GEO cartesian coordinates corresponding to every CPD record were deduced by an interpolation of the CPD time tags into ephemeris time values. This method resulted into numerically erroneous distances of the satellite to the center of the earth, even when the cartesian GEO coordinates for each record appear to be correctly (with an acceptable precision) interpolated. This is illustrated in Figure 1.1: the distances evaluated using the interpolated cartesian coordinates are lower than that deduced from the ephemeris GEO coordinates (see the bottom right panel). The correct way to perform position interpolation is by first converting the GEO cartesian coordinates into GEO spherical coordinates and second, to interpolate the time tags into these longitude, altitude and latitude tables. In Figure 1.2, the geographic coordinates deduced from such an interpolation are shown to fit well with the ephemeris GEO spherical coordinates (see the bottom panel). In general, the GEO cartesian coordinates extracted from the ephemeris file were converted into geographic, geodetic, (B,L) or magnetic coordinates tables, using the UNILIB library. The coordinates of each sample added to the data records were obtained by interpolation into these tables.

1.3 Statistical distribution of probed positions

In order to avoid biased interpretation which may result from non-uniform probing of the space domain covered by the ØRSTED satellite, the statistical distribution of the probed positions was analysed. For this purpose, the data acquired during april were used. The left column in Figure 1.3 shows the distributions of all latitudes, longitudes, altitudes, local time, magnetic field and L parameter probed by the ØRSTED/CPD. The samples appear to be uniformly distributed except the altitudes which display an oversampling around the apogee and perigee region, the local time, the B/B_0 and L coordinates.
The middle column represents the distributions of the above mentioned coordinates where the counting rates of channel P31 and P41 are greater than zero. Counting rates greater than zero in these channels indicate regions where high energy electrons ($E > 1\ MeV$) are encountered. The latitude histogram shows that high energy electrons are detected in the auroral as well as in the South Atlantic Anomalie (SAA) regions.
In the rightmost column, the coordinate distributions are constrained by the condition of counting rates greater than zero in channels P32, P33 P42 and P43 which is fulfilled in region with significant flux values for protons with energy higher than 10 MeV. One notices the sorting out of high energy protons in the South Atlantic Anomalie (SAA) region with a peak at about -25 deg. latitude and a less important but clearly discernible signal in the polar regions. The occurrence of high energy protons is altitude dependent.

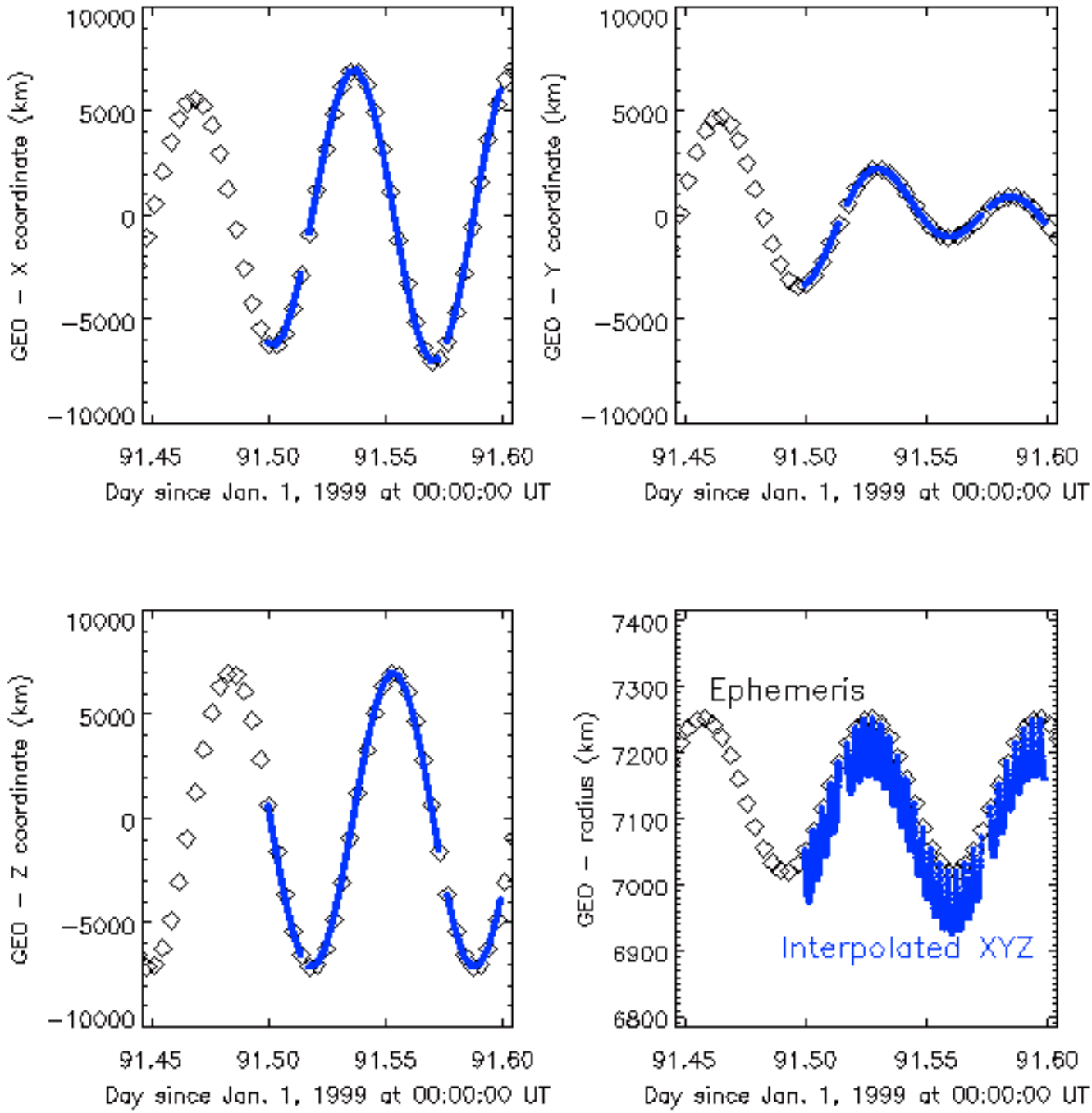

Figure 1.1: Interpolation of the CPD time tags for position evaluation (GEO cartesian coordinates).

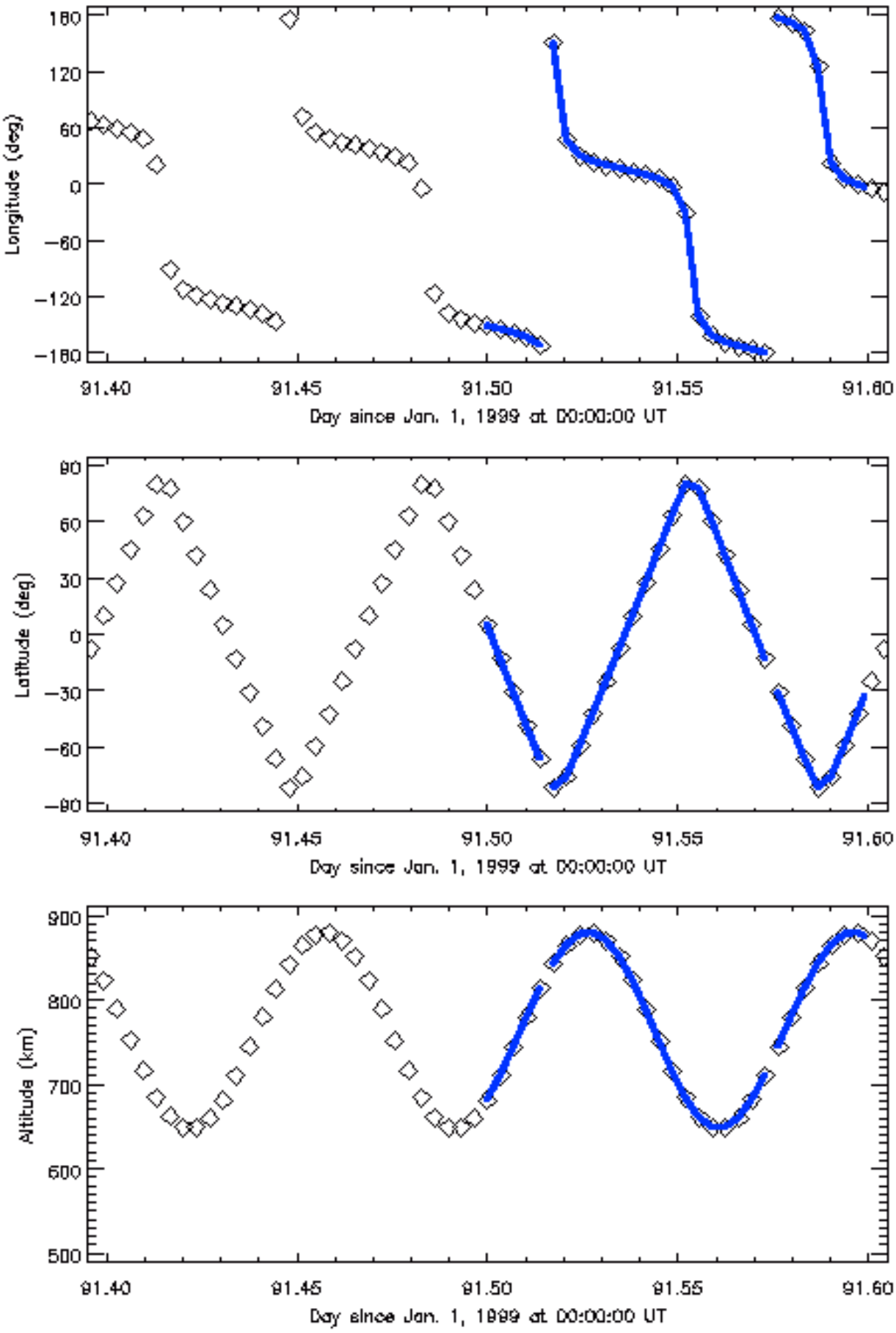

Figure 1.2: Interpolation of the CPD time tags for position evaluation (GEO coordinates).

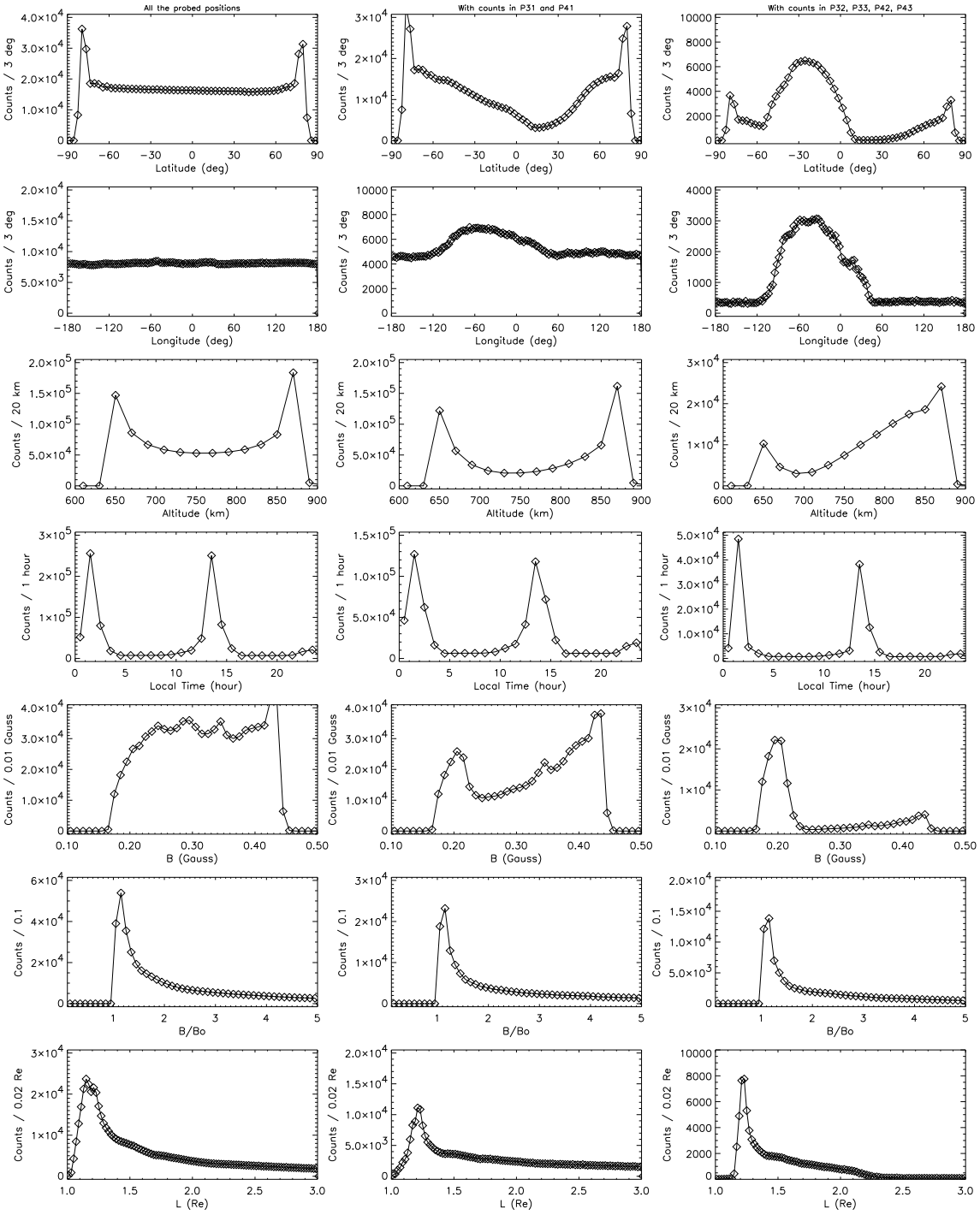

Figure 1.3: Distribution of positions coordinates probed by the ØRSTED/CPD. Note that the counts represented in the ordinate axis are not counting rates but number of occurence of the coordinate among the probed positions.

Chapter 2

The CPD intrinsic detection efficiency

The intrinsic detection efficiency of each of the 40 CPD channels was calculated for electrons (0.01 - 10 MeV), protons (0.1 - 300 MeV) and α-particles (0.4 - 300 MeV) using the GEANT 3.21 Monte-Carlo code: $25\ 10^5$ particles of a given species were initiated evenly over the 0.95 cm radius aperture of the P3 and P4 detectors or the 0.915 cm radius aperture of the E1 and P1 detectors. The incidence angle ranges from 0 to 90 degrees, by 2 degrees increment between 0 and 40 degrees. For every tracked particle the energy lost in the sensor was used to determine the recording channel. For each energy and angle, the ratio between the number of counts in a channel to the total number of initiated events was calculated. The results for incidence angles 0, 16 and 20 degrees are plotted in Figure 2.1, 2.2 and 2.3, respectively. We must stress that the energy and angular dependent intrinsic efficiency is the most general characteristic from which one may deduce particle fluxes using counting rates of any detector channel. While evaluating this detection efficiency function, no assumption was made about the energy nor the angular distribution of the particle fluxes. The functions displayed in Figure 2.1 to 2.3 may be used for any energy spectrum, for anisotropic flux as well as isotropic flux.
Also, it should be mentionned that the detection efficiency functions contain all the information about the detector field of view angle, the energy thresholds and the maximum energy of particles for each channel.

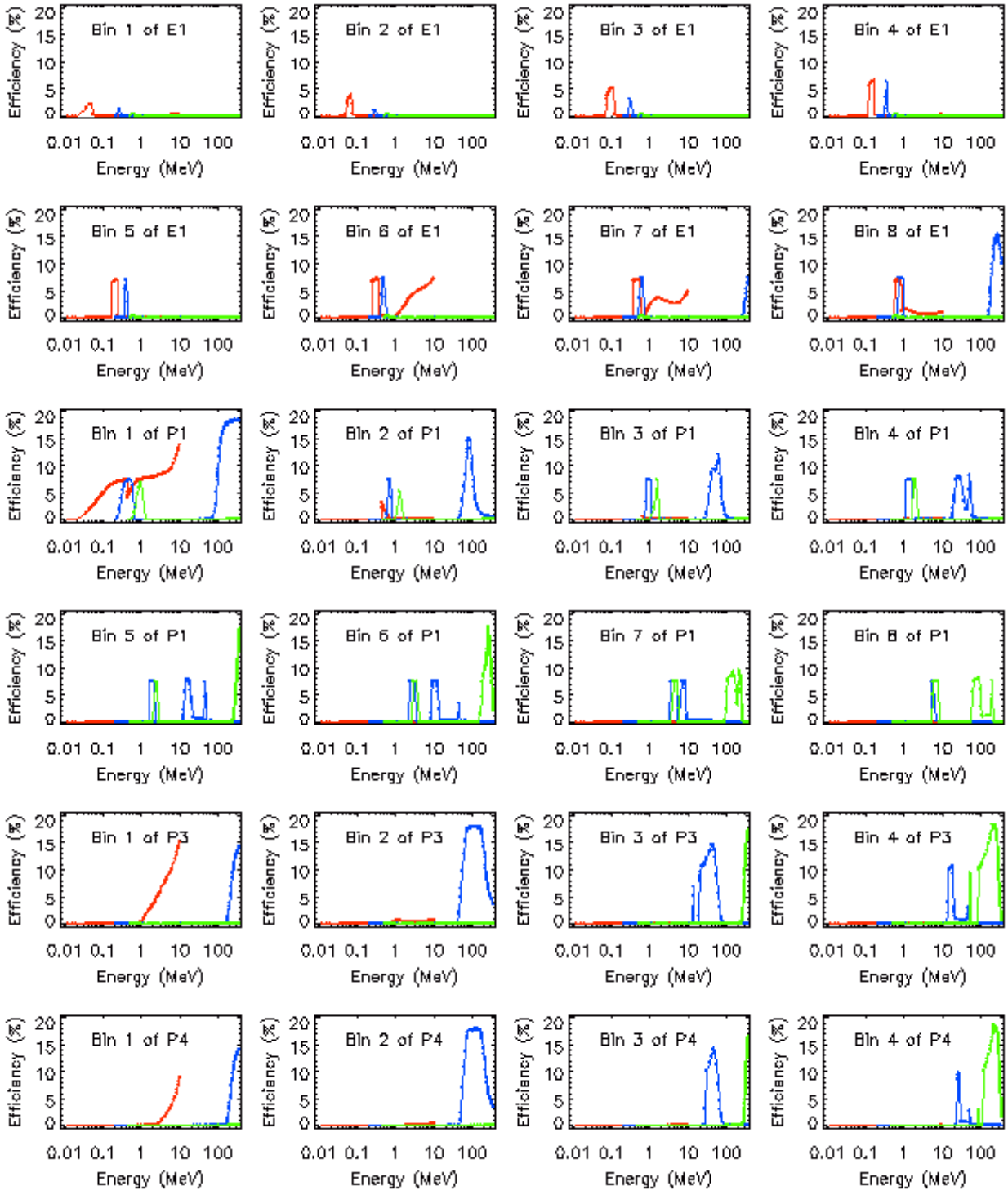

Figure 2.1: Energy dependent detection efficiency of all the "up-looking" CPD channels for electrons, protons and α - particles at a 0 deg. incidence angle.

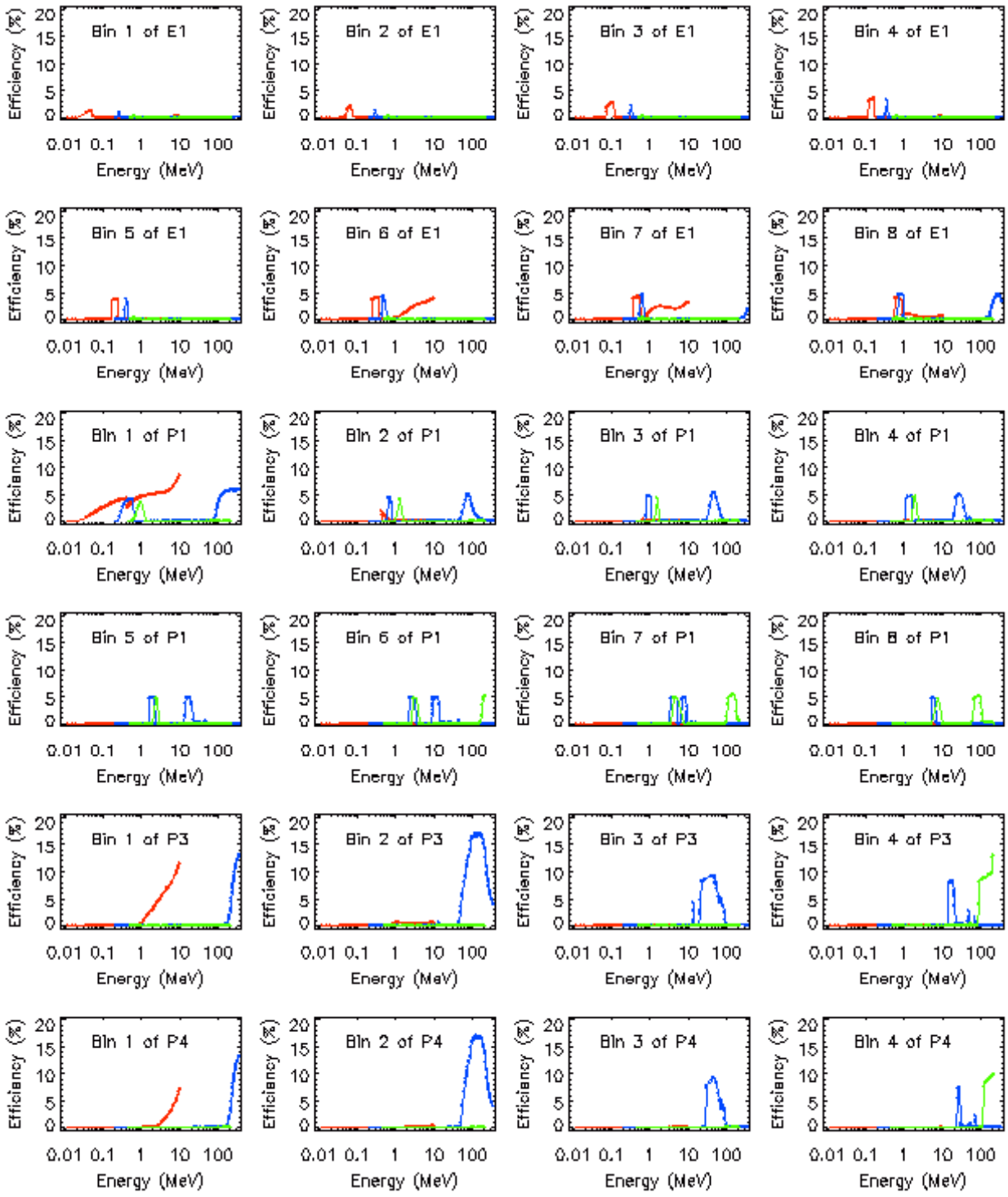

Figure 2.2: Energy dependent detection efficiency of all the "up-looking" CPD channels for electrons, protons and α - particles at a 16 deg. incidence angle.

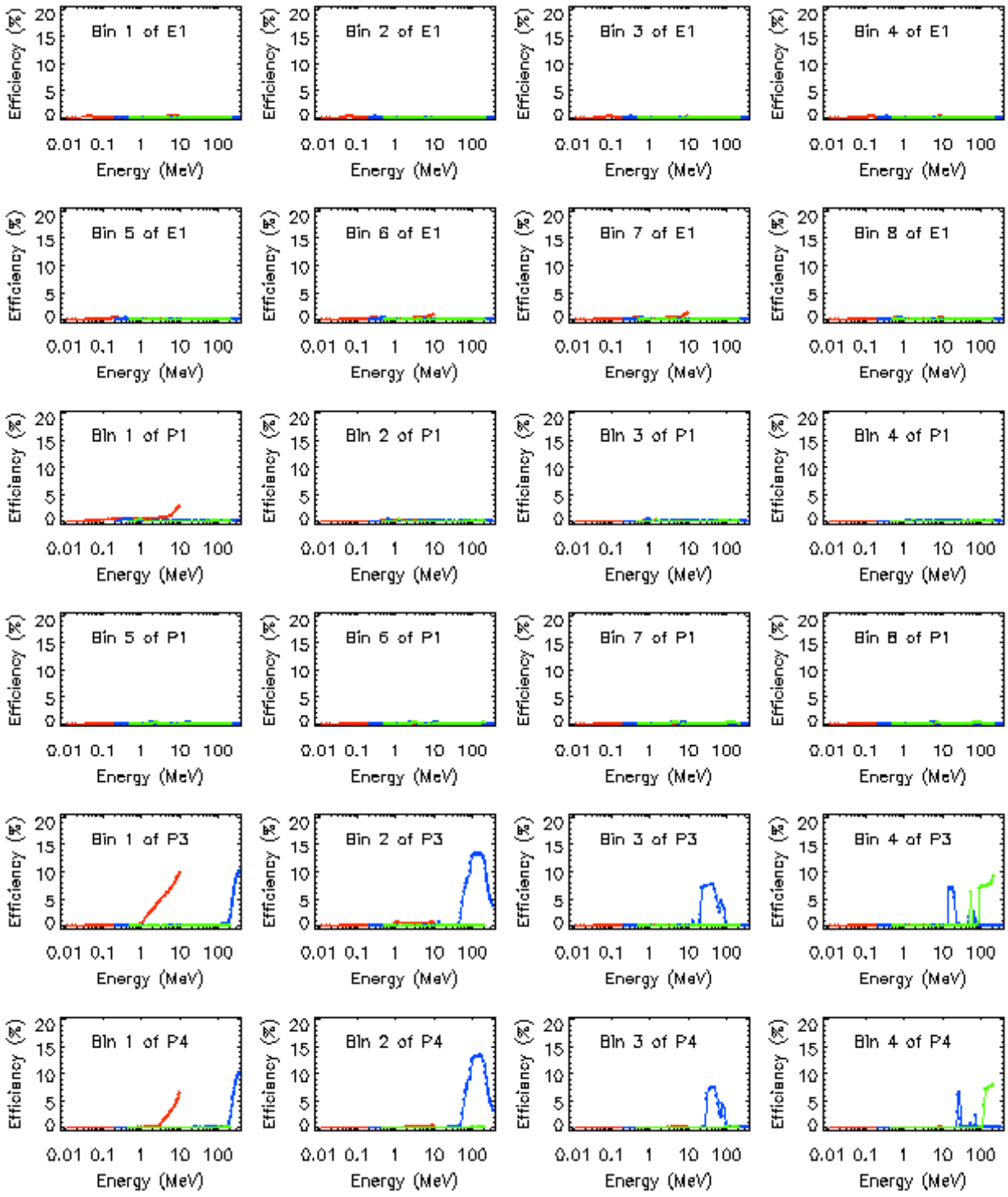

Figure 2.3: Energy dependent detection efficiency of all the "up-looking" CPD channels for electrons, protons and α - particles at a 20 deg. incidence angle.

Chapter 3

The CPD data analysis

3.1 Deconvolution of electron and proton spectra

The general expression of the time averaged counting rate of a detector or its channel is

$$N = \int_S dA \int_\Omega d\omega \int_{E_{th}}^{E_{max}} \epsilon(E, \vec{\sigma}, \omega) \phi_d(E, \omega) dE \tag{3.1}$$

where the functions $\epsilon(E, \vec{\sigma}, \omega)$ and $\phi_d(E, \omega)$ are the detection efficiency and the particle flux, respectively. The general detection efficiency is a function of the energy E, the position where a particle impacts the aperture surface $\vec{\sigma}$ and the incidence solid angle ω. The integral Equation 3.1 is carried out over the aperture surface domain S, the total solid angle Ω and the energy interval between E_{th} and E_{max}. dA is the effective surface looking into the solid angle element $d\omega$.
The angular and energy dependent particle flux is usually expressed as a product of the angular dependent function $F_d(\omega)$ and the energy dependent differential flux $J_d(E)$. On the other hand, when the detection system is not able to identify the impact position of a particle on the aperture surface, the averaged efficiency over the $\vec{\sigma}$ variable may be used to evaluate the counting rate using the expression

$$N = \int_\Omega d\omega \int_{E_{th}}^{E_{max}} F_d(\omega) J_d(E) dE \left[\int_S \epsilon(E, \vec{\sigma}, \omega) dA \right] \tag{3.2}$$

The integral into bracket may be rewritten as

$$h(E, \omega) = \frac{1}{A(\omega)} \int_S \epsilon(E, \vec{\sigma}, \omega) dA \tag{3.3}$$

which defines analytically the averaged intrinsic detection efficiency that we have defined and evaluated in Chapter 2. Inserting the Equation 3.3 in Equation 3.2, one gets

$$N = \int_\Omega \int_{E_{th}}^{E_{max}} F_d(\omega) A(\omega) h(E, \omega) J_d(E) d\omega dE \tag{3.4}$$

Using the definitions $d\omega = \sin\theta d\theta d\phi$ and $A(\omega) = A\cos\theta$ for a plan aperture surface the counting rate expression is simplified to

$$N = A \int_{\theta=0}^{\theta=\pi/2} \int_{\phi=0}^{\phi=2\pi} \int_{E=E_{th}}^{E=E_{max}} F_d(\omega) \sin\theta \cos\theta h(E, \theta) J_d(E) d\phi d\theta dE \tag{3.5}$$

a general expression for the counting rate that is reduced to

$$N = 2\pi A \int_{\theta=0}^{\theta=\pi/2} \int_{E=E_{th}}^{E=E_{max}} h(E,\theta) J_d(E) \sin\theta \cos\theta d\theta dE \qquad (3.6)$$

when the particle flux is isotropic ($F_d(\omega) = 1$).

Calculation of counting rates using the above equation is very time consumming. Equation 3.6 may be conveniently replaced by [6]

$$N = G \int_{E=E_{th}}^{E=E_{max}} p(E) J_d(E) dE \qquad (3.7)$$

where $G = \pi A$ is the aperture geometrical factor and the averaged efficiency $p(E)$ is defined as

$$p(E) = 2 \int_{\theta=0}^{\theta=\pi/2} h(E,\theta) \cos\theta \sin\theta d\theta \qquad (3.8)$$

Equations 3.6 and 3.7 are numerically equivalent provided that the function $h(E,\theta)$ is sampled at enough data in the (E,θ) domain. This was checked by comparing the angle-averaged efficiency function $p(E)$ obtained using Equation 3.8 and the average efficiency directly calculated using the GEANT code. The result is shown in Figure 3.1. It was concluded that the numerical evaluation

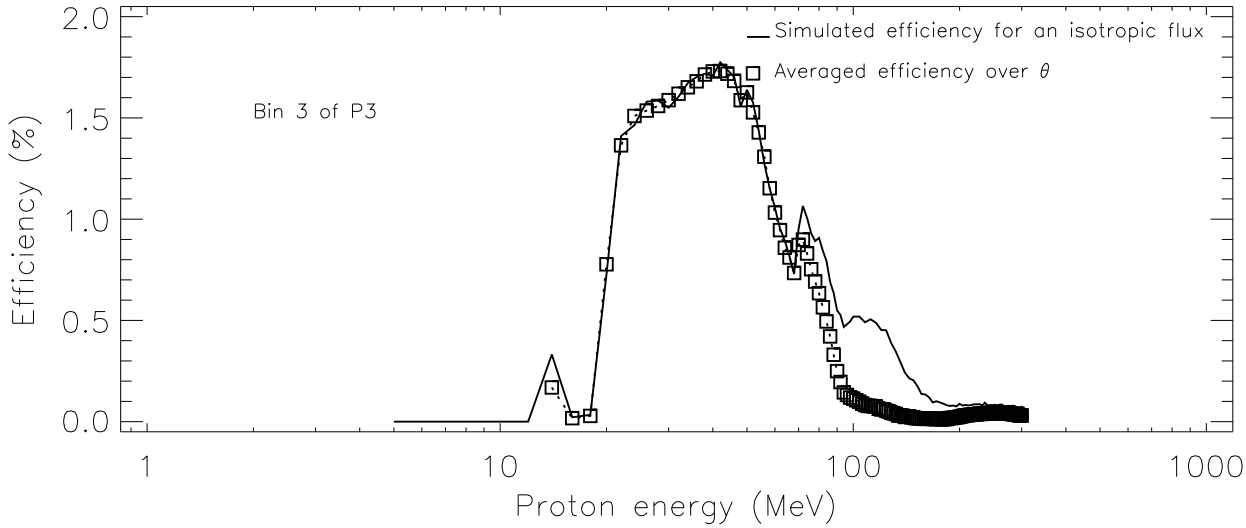

Figure 3.1: Comparison between the efficiency function based on Equation 3.8 and the GEANT results.

of the averaged efficiency function $p(E)$ may lead to underestimated values due to errors that occur during the evaluation of $h(E,\theta)$ by interpolation. Therefore, the angle-averaged efficiency to be used in case of isotropic particle fluxes was directly calculated for protons and electrons using the GEANT Monte-Carlo simulation code. The resulting efficiencies are shown in Figure 3.2. The counting rates specific to each detector channel will be noted $N_k(D_{ij})$, where $k = p\ or\ e$ are indexes of the particle type (proton or electron), $D = P\ or\ E$ indicates the detector type, i specifies the detector number and j the detector channel.

The electron and protons energy spectra (differential fluxes) are modelised by expressions of the form $J_d(E) = J_{d0}(E/E_0)^{-\gamma}$. The values of E_0 are 2 MeV and 59 MeV for electrons and protons, respectively. The model parameters J_{d0} and γ are obtained by a least-square fit method where

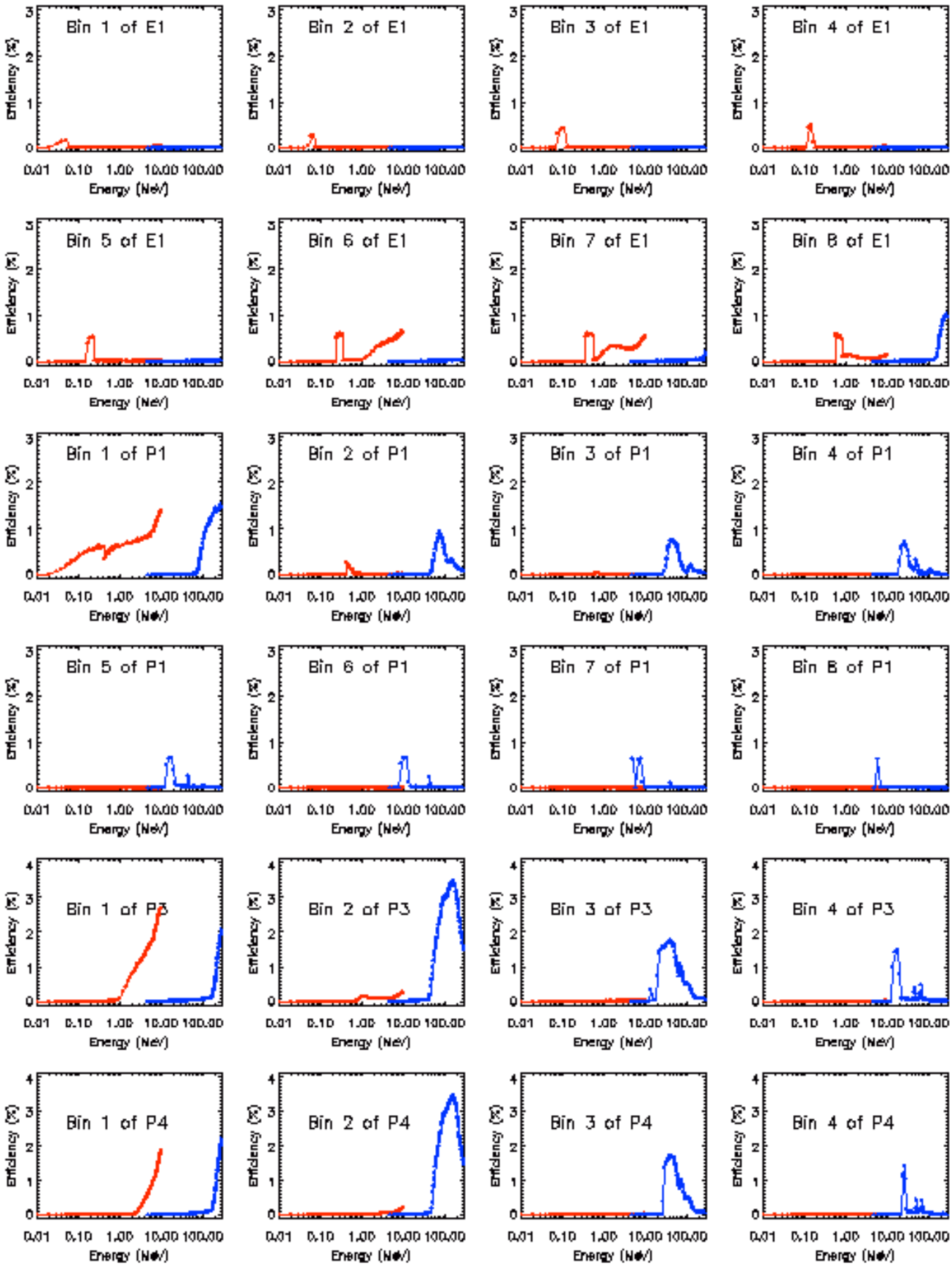

Figure 3.2: Angle averaged efficiencies of the CPD channels for isotropic electron and proton fluxes.

observed counting rates are compared to predicted ones (see Equation 3.6). The experimental parameters correspond to the minimum of the function:

$$F = \sum_{i=3}^{4} \sum_{j=1}^{3} \frac{(N_T(P_{ij}) - N_T^{obs}(P_{ij}))^2}{N_T^{obs}(P_{ij})} \tag{3.9}$$

where $N_T(P_{ij}) = N_e(P_{ij}) + N_p(P_{ij})$ is the total contribution of electrons and protons to the counting rate in channel P_{ij} of the detector P_i. Only the detectors P3 and P4 were used because their channels achieve a relatively good particle species discrimination, making easy the deduction of spectrum parameters. Data from the detectors P1 and E1 may be added in this deconvolution process at the expense of a dramatic increase of the calculation time. Finally, the detectors P2 and E2 (looking into a direction perpendicular to that of detectors P1 and E1) will not be used unless reliable attitude data are made available and more computer resources are installed.

3.2 Rough estimates of particle fluxes

The maximum value of the P42 efficiency for protons with energy above 60 MeV is 3.5%. The number of protons reaching the P4 aperture per second is the product of the geometrical factor $G = \pi A = 8.9 cm^2 sr$ by the integral flux $J(E > 60MeV)$. The lower limit of proton flux $J_{min}(E > 60MeV)$ may be deduced from the counting rate of the P42 channel using the expression

$$CR = G\epsilon_{max} J_{min}(E > 60MeV) = 0.31 J_{min}(E > 60MeV) \tag{3.10}$$

This proton flux lower limit is expressed in $cm^{-2}\ sec\ sr$ units.

A value for the P3 and P4 geometrical factor equal to $0.25\ cm^2 sr$ was given in Table 1. It resulted from an approximate formula of the geometrical factor of a two-element telescope [5] as

$$\frac{A_1 A_2}{R_1^2 + R_2^2 + l^2} \leq G \leq \frac{A_1 A_2}{l^2} \tag{3.11}$$

where A_1, A_2 and l are the areas of the elements and the distance separating them, respectively. R_1 and R_2 are the radius of the circular telescope elements.

Although we commend the use of the thorough method described in Section 3.1 to extract fluxes from counting rates or the Equation 3.10 to get a lower limit of the fluxes, the P42 counting rate formula $CR \approx 0.25 J(E > 60MeV)$ may be used at least to get an order of magnitude of the proton flux.

Chapter 4

Proton and electron spectra detected by the ØRSTED/CPD

The data analysis method decribed above was applied to the CPD data acquired during April 1999. The whole data set available to us may be processed at will using the same computer codes. The resulting fluxes are presented hereafter, separately for protons and electrons. The measured fluxes are presented as a function of time, space position along with characteristics of the spectra. We have paid a particular attention to the high energy ($E > 60\ MeV$) proton flux that may have induced the high SEU rate detected by the Error Detection And Correction (EDAC) system. The CPD results were compared to predictions of AP8-MAX and AE8-MAX when applicable.

4.1 Application example

Below is a brief description of CPD data processing. The considered record was acquired on April 11, 1999 at 15:07:11.4 UT. Its time tag along with the counts during 2 seconds are listed below:

```
============================================================
year month day hour minute sec xxx xxx xxx livetime

 99  4 11 15  7 11.400  17  36  47438   2000
    3880    1464     868     520     304     148      64      30 E1
   92160   84992   69632   36992   21376    7616    1928    1272 P1
    2576    1480     324      37                              P4
    2688    1488     354      38                              P3
    6464    2000    1120     626     348     175      75      27 E2
  138240  128256  105984   58112   34176   11872    2760    1640 P2
============================================================
```

The satellite geographical position (-17.59 deg. latitude, -18.86 deg. longitude and 824.49 km altitude) was determined by interpolating the record time into the ephemeris table (see an extract below).

```
  Time (UTC)       x         y         z         vx        vy        vz      alt      lat      lon     mlat  ...
19990411 15:00  5176.464 -1209.836 -4905.365  4.416668 -2.592831  5.395890  865.126 -42.8915  -13.1550 -44.60 ...
19990411 15:05  6221.695 -1943.515 -3080.526  2.495453 -2.244663  6.675315  835.248 -25.4446  -17.3476 -33.55 ...
```

```
19990411 15:10  6649.720 -2525.555  -962.700  0.335079 -1.587020  7.331164  800.271  -7.7589  -20.7967 -20.76 ...
19990411 15:15  6419.856 -2869.693  1247.586 -1.853746 -0.670340  7.283294  764.379  10.1268  -24.0848  19.12 ...
```

The ØRSTED positions as a function of the geographic and geodetic coordinates (used as input in SPENVIS/AP8) are listed below:

```
Day1999     GEOLAT  GEOLON GEOALT  GDELAT  GDELON  GDEALT

100.629947 -17.827 -18.812 824.912 -17.926 -18.812 819.965
100.629970 -17.709 -18.835 824.702 -17.808 -18.835 819.730
100.629993 -17.592 -18.858 824.493 -17.690 -18.858 819.495 (our focus)
100.630016 -17.475 -18.881 824.283 -17.573 -18.881 819.260
100.630039 -17.358 -18.904 824.073 -17.455 -18.904 819.025
```

In Table 4.1 the observed counting rates are compared to the results from the CPD models obtained by least-square fit of counting rates. Also, the CPD proton fluxes are compared to the predictions from AP-8 MAX.
On April 27, 2001, the SAMPEX/PSB97 and CRRESPRO proton models were added to the SPENVIS. However, no flux evaluation at a single position was allowed by the new model user's interface yet. Comparison of the CPD results with the SAMPEX/PSB97 predictions presented further in this chapter are based on SPENVIS fluxes evaluated at sample positions along the ØRSTED orbit. The proton flux deduced from the CPD counting rates are much higher than

Day since 1 Jan. 1999:	*100.6300*
Latitude:	*-17.59*
Longitude:	*-18.86*
Altitude:	*824.49*
P31 observed counting rate:	*1344*
P31 model counting rate:	*1568*
P32 observed counting rate:	*744*
P32 model counting rate:	*806*
P33 observed counting rate:	*177*
P33 model counting rate:	*173*
P41 observed counting rate:	*1288*
P41 model counting rate:	*805*
P42 observed counting rate:	*740*
P42 model counting rate:	*732*
P43 observed counting rate:	*162*
P43 model counting rate:	*145*
Proton diff. flux at $E = 59\ MeV$*:*	*14.5*
Power law index (proton spectrum):	*0.2*
AP8-MAX omni. flux of $60 < E < 300\ MeV$ *protons (SPENVIS):*	*167*
AP8-MAX uni. flux of $60 < E < 300\ MeV$ *protons (SPENVIS):*	*656*
CPD integral flux of $60 < E < 300\ MeV$ *protons:*	*2843*
CPD lower limit integral flux of $60 < E < 300\ MeV$ *protons Equation 3.10:*	*2387*

Table 4.1: CPD results and comparison with model predictions. All the integral fluxes are expressed in $cm^{-2}\ sec^{-1}\ sr{-}1$.

the SPENVIS/AP8 predictions. We recall that the SPENVIS omni result corresponds to a pitch

angle averaged flux, whereas the unidirectional model gives the flux about 90 deg. pitch angle which is a maximum value as far as East-West asymetry is not taken into account.

Consider that all the protons having an energy above 60 MeV are counted by the CPD channel P42, even when they come from the back side of the satellite. This would be the case if the CPD sensor P4 is shielded over a 4π solid angle by a material equivalent to a 1 mm copper plate (which is equivalent to an aluminum proton shield of 2.6 mm). In such a case, a geometrical factor value $G = 2\pi A = 3.16 cm^2 sr$ (where $A = 50\ mm^2$ is the sensor area) should be used to roughly deduce integral fluxes from the P42 counting rates. For the position considered in Table 4.1, the integral flux corresponding to $740\ Hz$ counting rate value is about $235\ cm^{-2} sr^{-1} sec^{-1}$ (to be compared to the $167\ cm^{-2} sr^{-1} sec^{-1}$ SPENVIS omni. result). We see that even in this case where the CPD sensors are considered as insufficiently shielded, the observed counting rate values correspond to a proton flux higher than AP-8 predictions. In other words, even if the P4 sensor was not sufficiently shielded, an AP-8 MAX flux of $167\ cm^{-2} sr^{-1} sec^{-1}$ would lead only to a counting rate value of $528\ Hz$ which is less than the observed counting rate.

4.2 Proton flux along the ØRSTED orbit

4.2.1 Time variation of the proton flux

Information on the location of the high-energy proton-rich SAA region at the ØRSTED altitude may be found in Figure 1.3. In order to compare the actual SAA location to the AP8 prediction, the high energy proton flux was plotted as a function of time. In Figure 4.1, the positions of the maximum of AP8 high energy protons appears to coincide fairly well with the CPD measured one. Also the AP8-predicted size (or extension in space) of this region of high energy protons is equivalent to the actual one. However, on the basis of the analysed data, the proton flux measured using the CPD appears to be an order of magnitude higher than the AP8-MAX (omnidirectional) predictions. In the lower panel of Figure 4.1, the uncertainty on the CPD fluxes (red) are represented by the error bars (black). Typically this uncertainty amounts to 30%.

We have had to resort to several methods to evaluate the AP8 high energy proton fluxes. The results shown in Figure 4.1 were obtained using the UNIRAD user's interface, whereas the Figure 4.3 was obtained using the SPace ENVironment Information System (SPENVIS) for radiation evaluation on the ØRSTED orbit. On the other hand, the CPD data were analysed not only using the thorough method described in the previous chapter, but also by use of the rough method which gives a lower limit of the integral flux of high energy protons. Both methods confirm that the proton flux is by an order of magnitude underestimated in the AP8-MAX model, along the ØRSTED orbit.

Predictions from the CRRESPRO models (based on the data from the PROton TELescope flown aboard the CRRES satellite) were also compared to the CPD results. It is noticed that the maximum flux predicted by CRRESPRO (see Figure 4.2) along the ØRSTED orbit is also a factor 2 or so, lower than the CPD counterpart. The CRRES satellite launched on July 25^{th}, 1990 had an orbit of a 350 km perigee, 35000 km apogee and 18 deg. inclination. Therefore, it did not fly over the SAA latitudes. The CRRESPRO model uses drift shell informations and extrapolations to evaluate fluxes at positions not covered by the CRRES satellite. Finally, the SAMPEX/PSB97 proton fluxes accessed through the SPENVIS were compared to the CPD results. Since the orbit

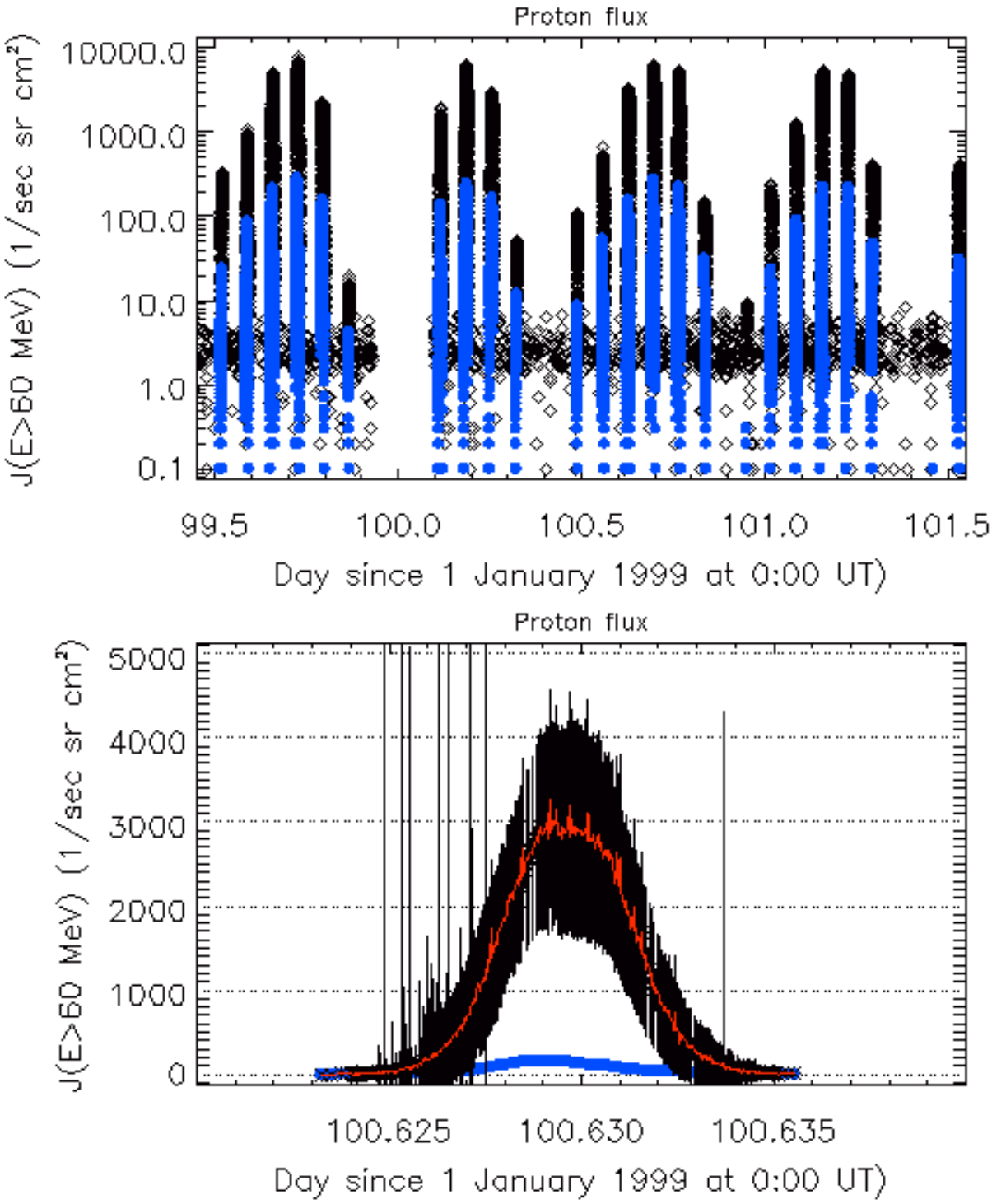

Figure 4.1: High energy proton flux as a function of time, showing that the peaks of fluxes measured by the CPD (black, red) occur at the same time (position) as that predicted using the omnidirectional AP8-MAX model (blue).

(520 km perigee, 670 km apogee and 82 deg. inclination) of this satellite launched on July 3rd, 1992 brought it in the SAA region, the comparison of the PET fluxes to the CPD results seems more appropriate. However, it may be argued that the PET sampled proton fluxes during a solar minimum period, which implies that differences between the CPD and the PET results would not be surprising. By comparing the omnidirectional AP8-MAX and AP8-MIN fluxes shown in Figure 4.3, we can evaluate the induced effect of the solar activity on proton fluxes along the ØRSTED orbit. This effect appears to be much lower than the order of magnitude discrepency

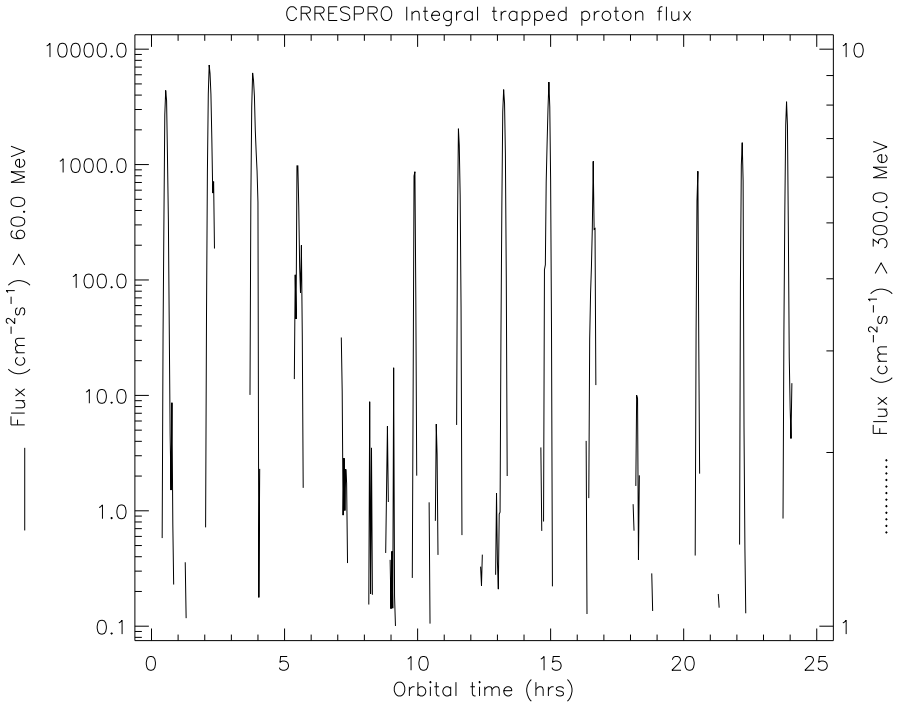

Figure 4.2: Proton flux $J(E > 60MeV)$ predicted by CRRESPRO QUIET model.

observed between the CPD results and AP8 models. The proton fluxes along the ØRSTED satellite deduced from the SAMPEX/PSB97 model are plotted as a function of time in Figure 4.4. As can be seen by comparing these results to that of Figure 4.1, the SAMPEX/PSB97 maximum proton fluxes are at most only a factor 2 lower than the maximum of CPD fluxes.

4.2.2 Daily averages of the proton flux

The dynamic of protons along the ØRSTED orbit was also investigated (see Figure 4.5). Averages of the integral flux of high energy protons detected by the CPD is compared to AP8 predictions. The bin sizes are 1 day and 1 deg. in magnetic latitude. The proton flux observed using the CPD is much higher than predicted by AP8. It may be noticed that an increase in the proton flux occured on day 98 (9 April 1999). The CPD was turned on at April 2 and remained during the first few days in a mode with reduced high-voltage bias ($\sim 75\%$ of the full bias) on the detectors. This slightly reduced the pulse amplification and lowered the depletion depth of the detector units.

The spectra characteristics $J_d(E = 59MeV)$ and the power law index display the same steep change of their values on Day 98 (see Figure 4.6). However, looking at the Kp and Dst indices for April 1999 in Figure 4.7, one finds no event which may have induced such an increase in the high energy proton flux. Of course some other indices correlated to increases in high energy protons may be checked, but also possible change in the operation mode of the CPD should be investigated.

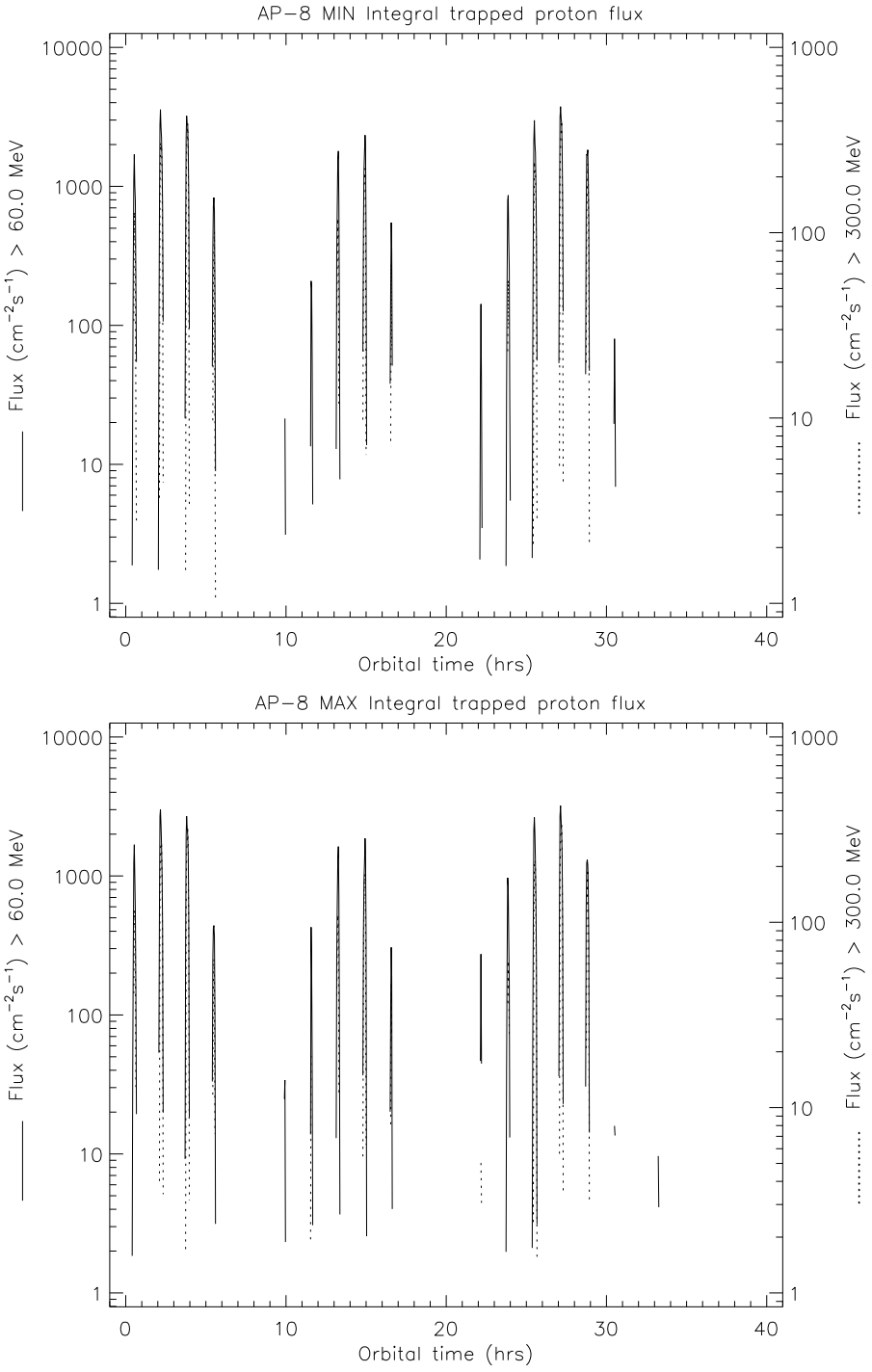

Figure 4.3: AP8-MIN (upper panel) and AP8-MAX (lower panel) predictions of high energy proton fluxes as functions of time along the ØRSTED orbit (divide the flux by 4π to convert it into $cm^{-2}sr^{-1}s^{-1}$).

4.2.3 Time averaged characteristics of the proton flux

It is well known that high energy protons may contribute to the SEU rates induced in electronic components onboad satellites. It has been found that the cosmic ray contribution to the SEU rate along the ØRSTED satellite evaluated using the CREME software is an order of magnitude lower than the observed SEU rate [3]. Also, according to CREME, protons do not contribute to SEU in the ØRSTED satellite components. Therefore, it was considered of great interest to

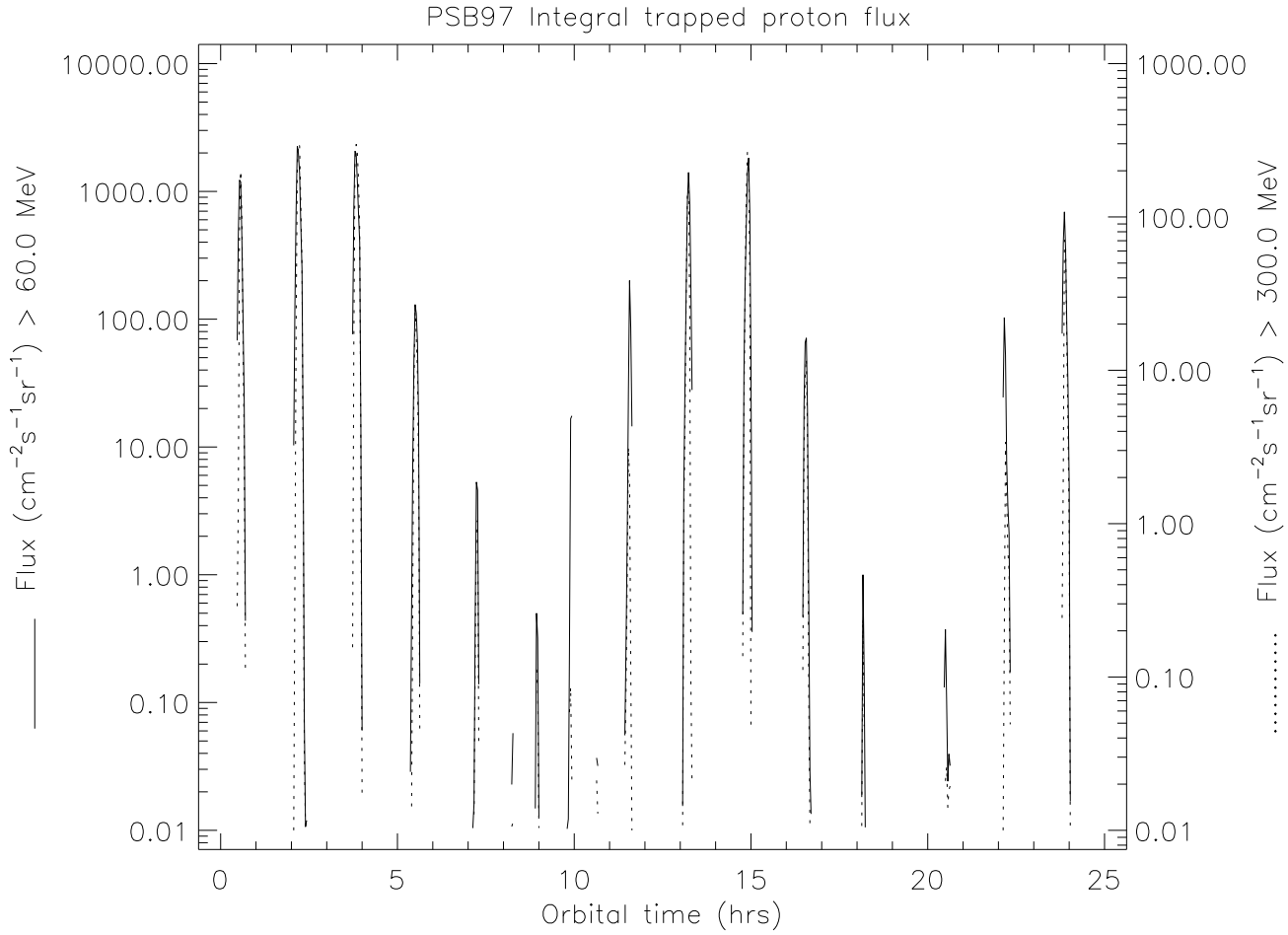

Figure 4.4: Proton flux $J(E > 60MeV)$ predicted by SAMPEX/PSB97 model.

determine precisely the flux of high energy proton along the ØRSTED orbit and to compare it to the AP8, CRRESPRO or SAMPEX/PSB97 predictions: The flux of protons with energy higher than 60 MeV measured by the CPD is shown in Figure 4.8. These results are compared to AP8-MAX predictions (shown in Figure 4.9) obtained using the UNIRAD library. The distribution of protons over the world map are shown in the Figure 4.10 to 4.13. The fluxes deduced from the CPD are compared to predictions from SAMPEX/PSB97, CRRESPRO and AP8-MAX. The peak fluxes of high energy protons deduced from the CPD is a factor 2 higher than the peak fluxes from the SAMPEX/PSB97 model. The CRRESPRO fluxes are about a factor 3 higher than the omnidirectional AP8-MAX predictions. The high energy proton fluxes deduced from the CPD are one order of magnitude higher than the AP8 predictions.

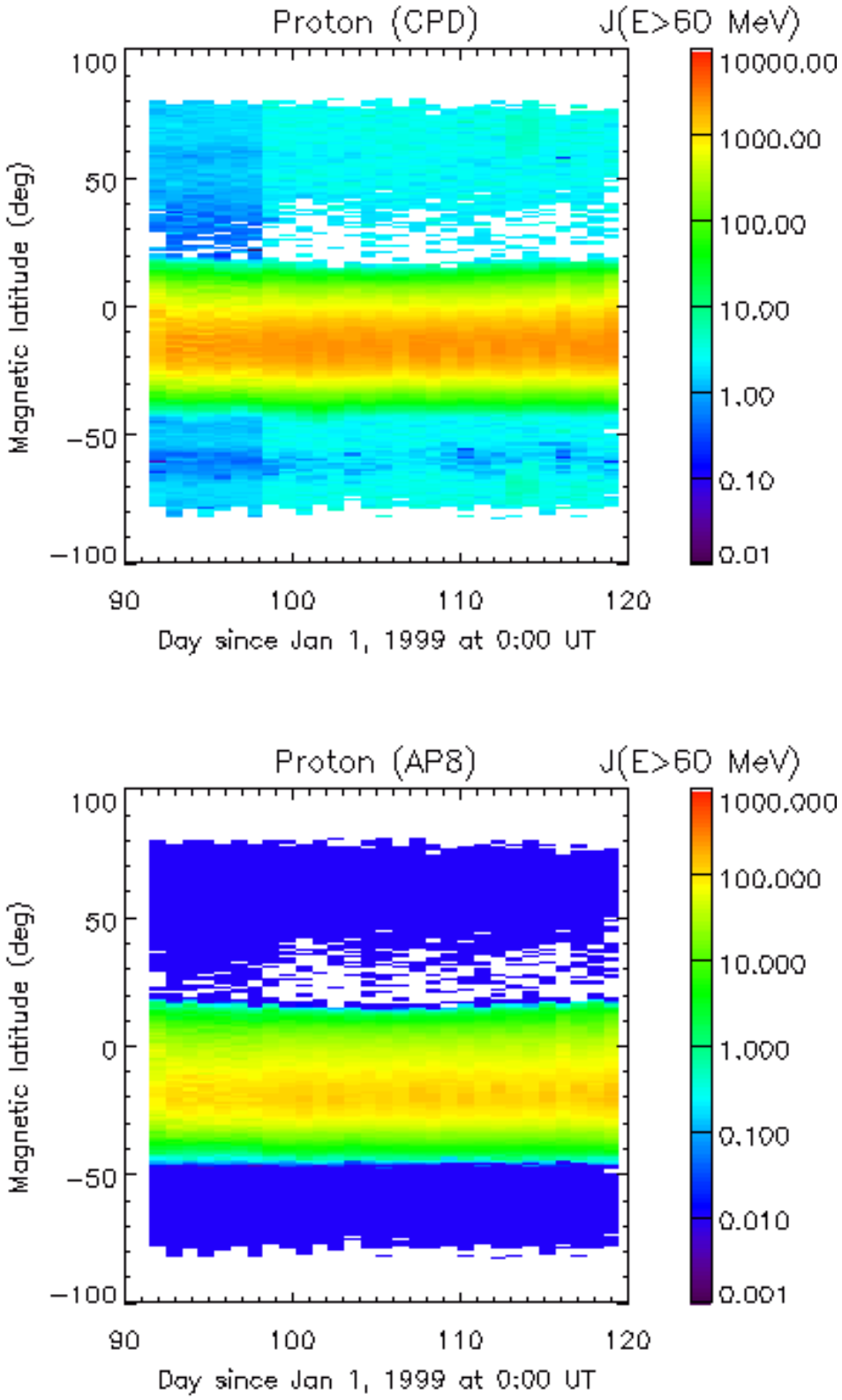

Figure 4.5: Proton flux $J(E > 60MeV)$ detected by the CPD compared to omnidirectional AP8-MAX predictions.

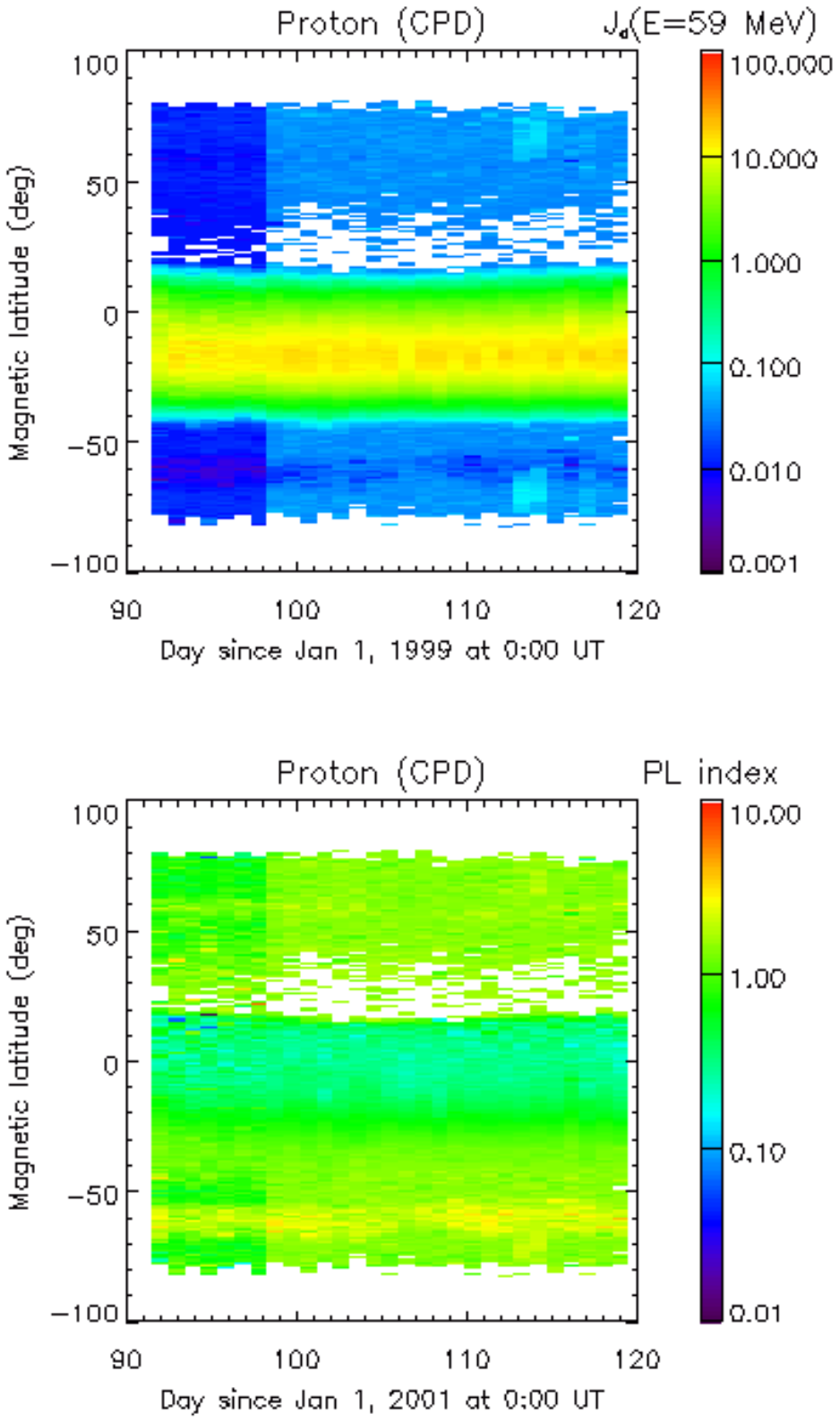

Figure 4.6: Proton differential flux $J_d(E = 59MeV)$ and power law index measured by the CPD.

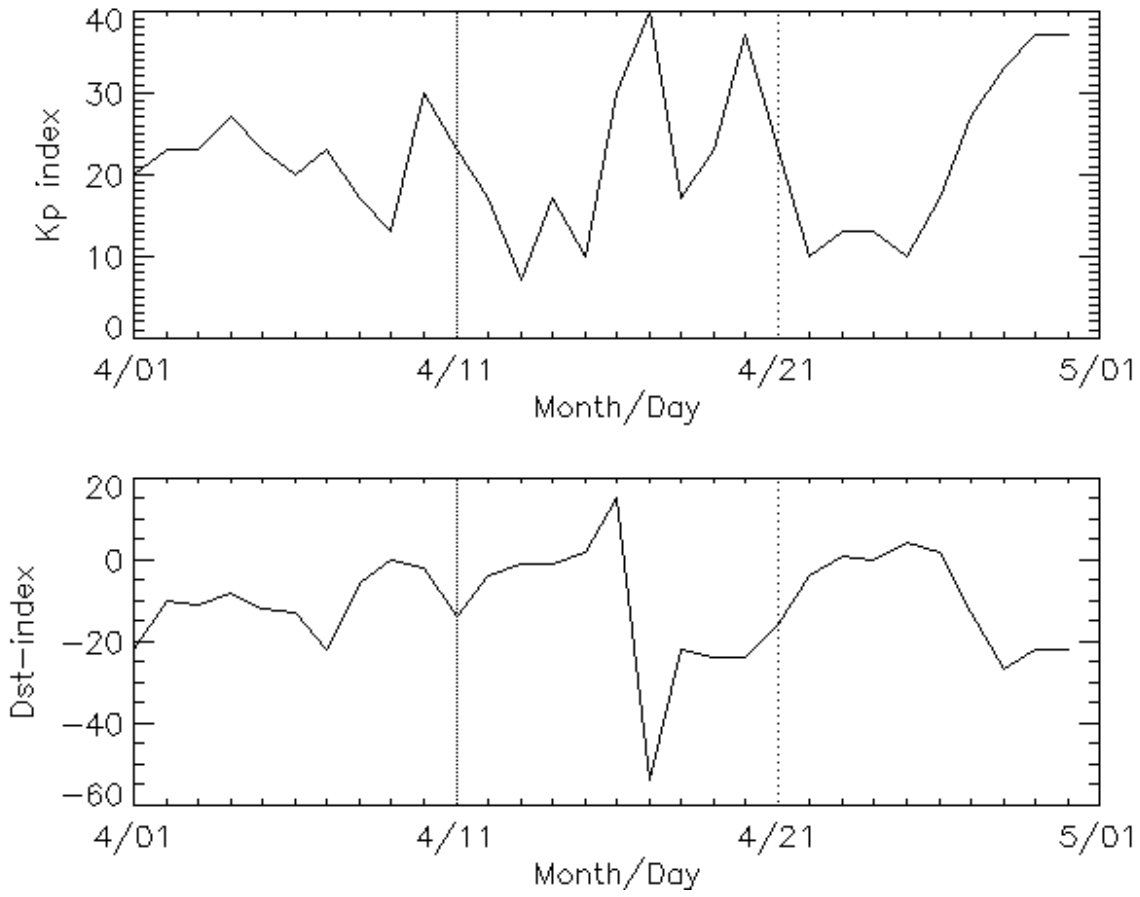

Figure 4.7: Kp and Dst index for April 1999. No major magnetospheric event related to Kp or Dst change on April 9, 1999 (Day 98, since 1/1/1999.

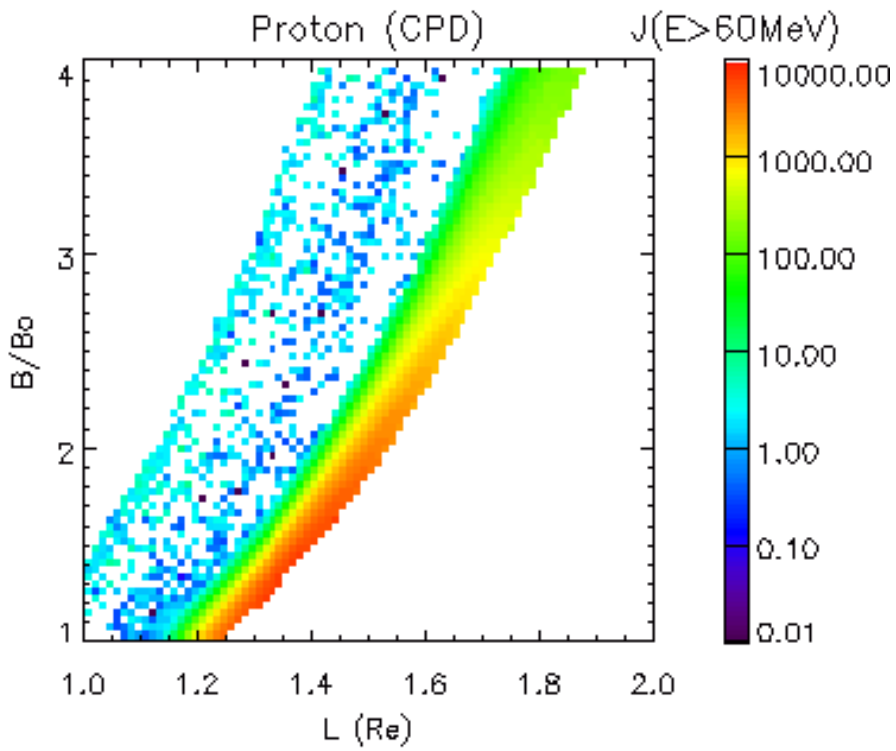

Figure 4.8: Proton flux $J(E > 60MeV)$ measured by the CPD.

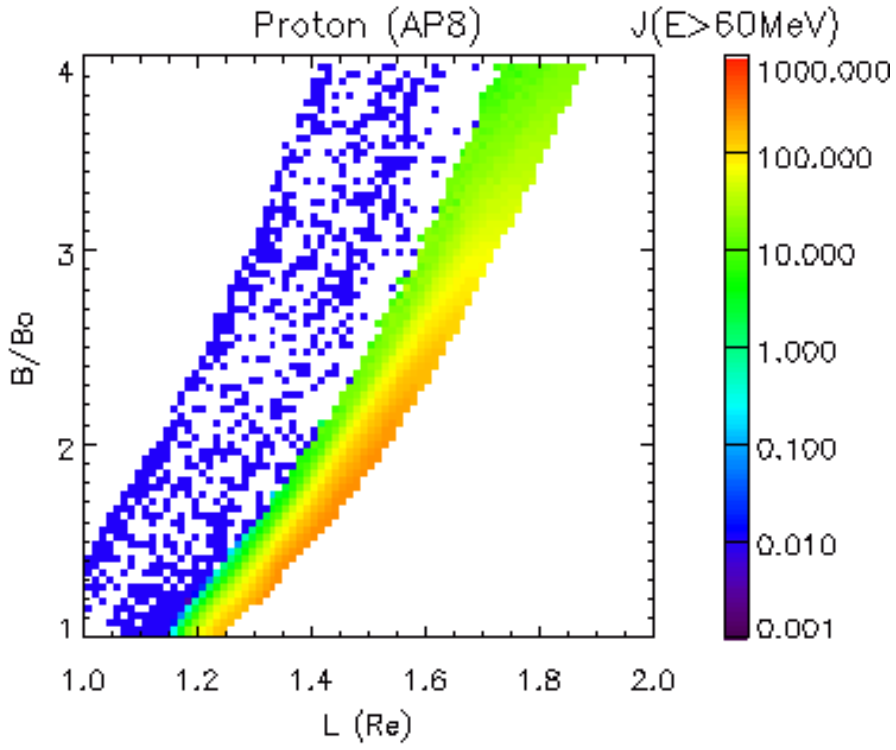

Figure 4.9: Proton flux $J(E > 60MeV)$ predicted using the UNIRAD library.

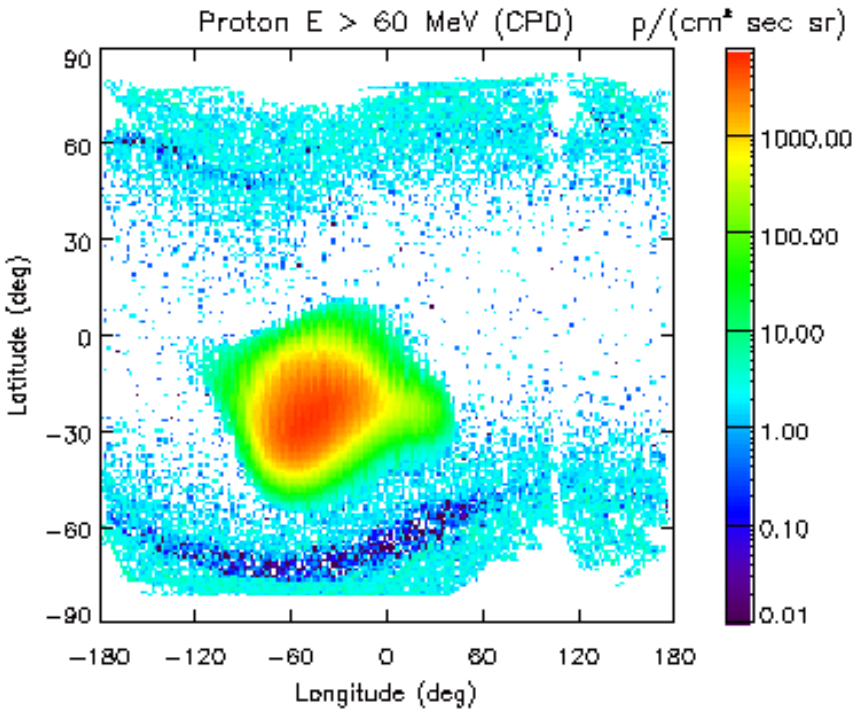

Figure 4.10: Proton flux $J(E > 60MeV)$ measured by the CPD.

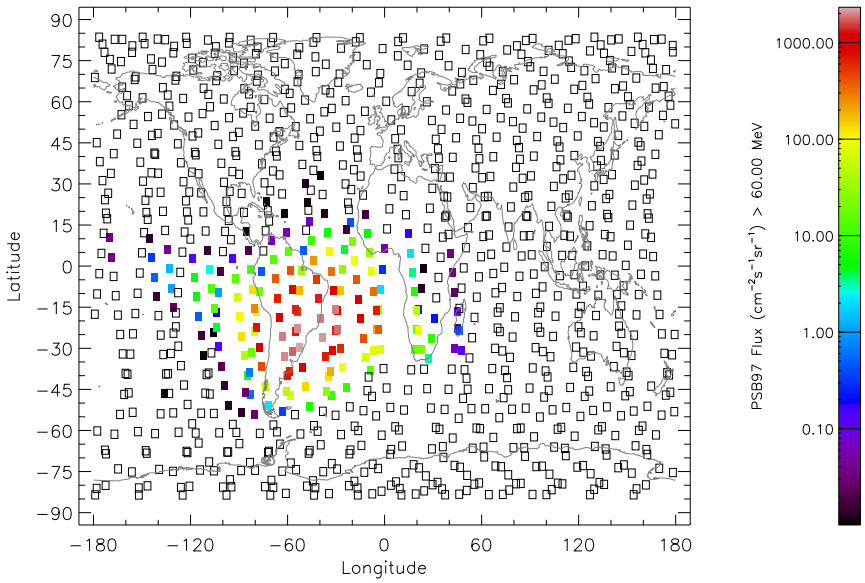

Figure 4.11: Proton flux $J(E > 60MeV)$ predicted by the SAMPEX/PSB97 model.

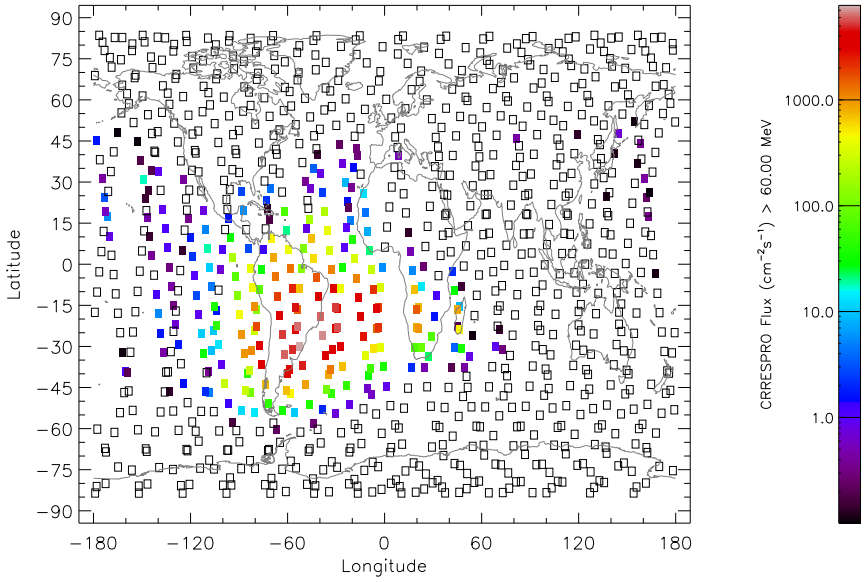

Figure 4.12: Proton flux $J(E > 60MeV)$ predicted by the CRRESPRO QUIET model.

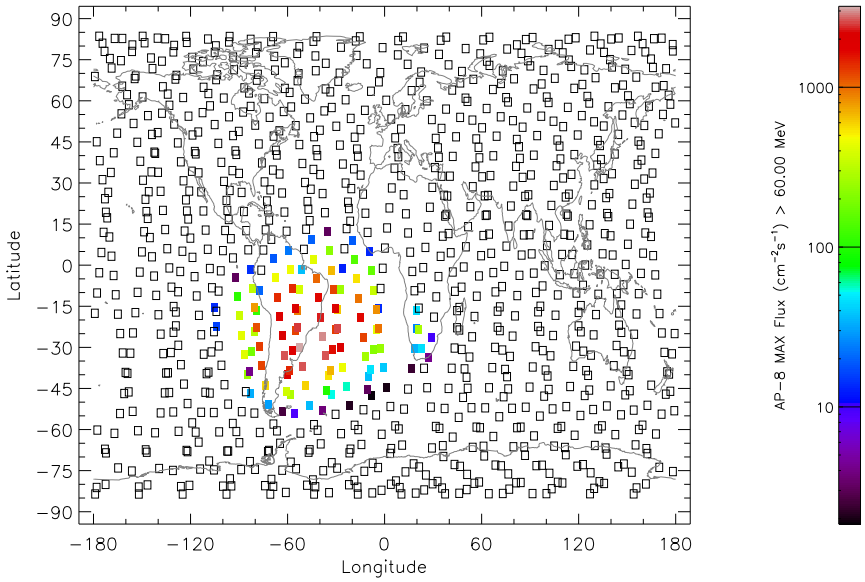

Figure 4.13: Proton flux $J(E > 60MeV)$ predicted by the AP8-MAX model.

4.3 Electron flux along the ØRSTED orbit

4.3.1 Time variation of the electron flux

The integral electron flux $J(E > 1MeV)$ detected by the CPD during successive passes accross the SAA and polar regions are shown in Figure 4.14. Contrarly to what was observed for high energy protons, the space extention of the electrons detected by the CPD is larger than predicted by the AE8-MAX model and the position of maximum flux are different. However, the maximum value of the electron flux predicted by the AE8-MAX model appears to be less underestimated than it was found for high energy protons.

4.3.2 Daily averaged electron flux

The integral flux of high energy electrons $J(E > 1MeV)$ is shown in Figure 4.15 where it may be compared to AE8-MAX predictions. Not only the AE8 peak flux location is shifted toward the south relatively to the CPD results, but also the AE8 model predicts higher electron fluxes in the auroral ovals than in the SAA. Also the latitude extend of the AE8 trapped electrons reaching the SAA region is reduced as compared to the CPD observations. Finally, as far as the positions where electrons are encountered are concerned, the counting rates measured by the CPD/P11 channel may be used. This channel may counts with more or less efficiency all the electrons with an energy higher than 0.02 MeV. A map of the raw CPD/P11 counting rates is shown in Figure 4.16 and confirms the above statements on the electrons location.

4.3.3 Time averaged electron fluxes

The Figure 4.17 shows high energy electron fluxes predicted by AE8 and its CPD measured counterparts.

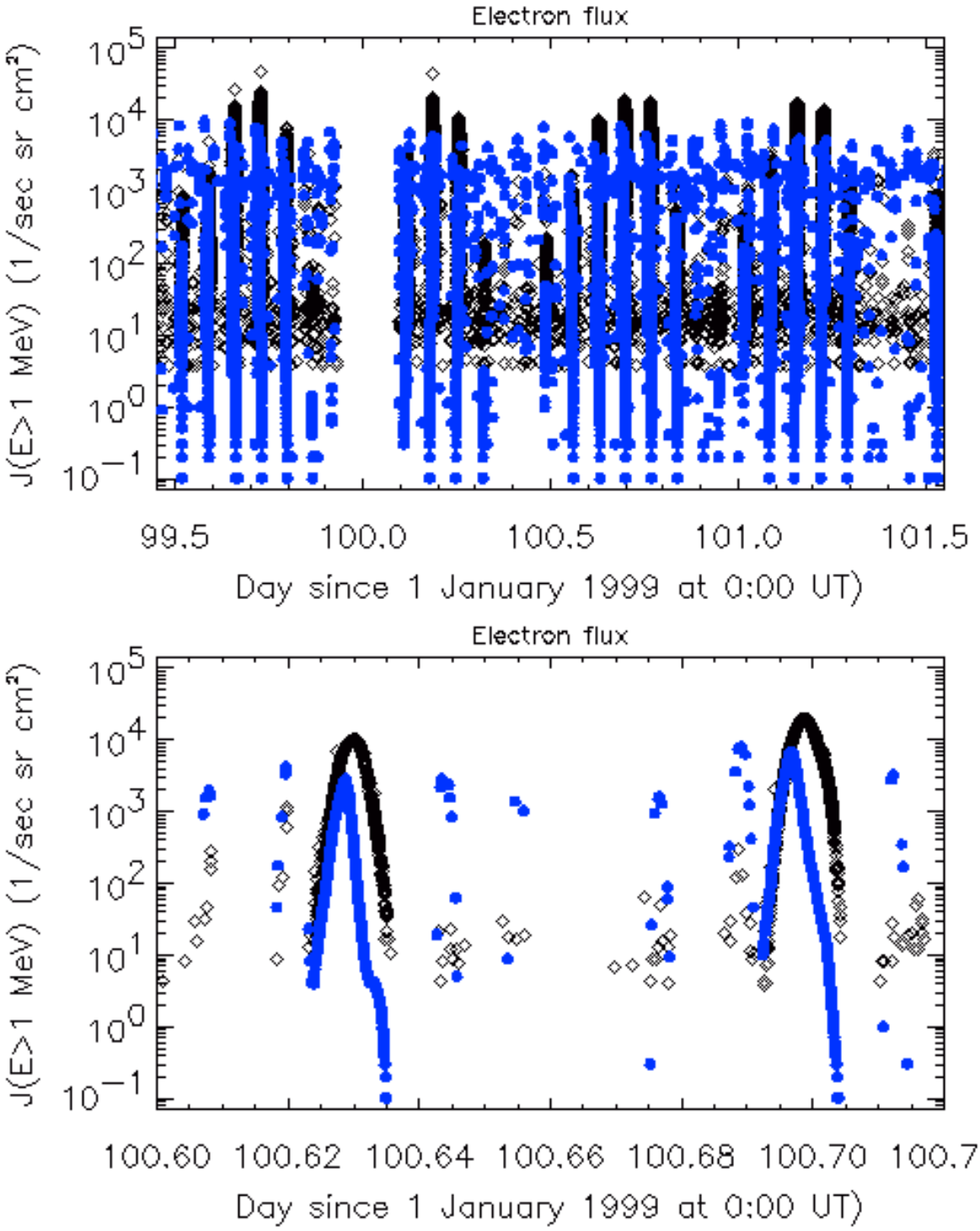

Figure 4.14: High energy electron flux as a function of time, showing that the CPD flux peak (black) occurs at a different time (position) than that predicted by AE-8 (blue).

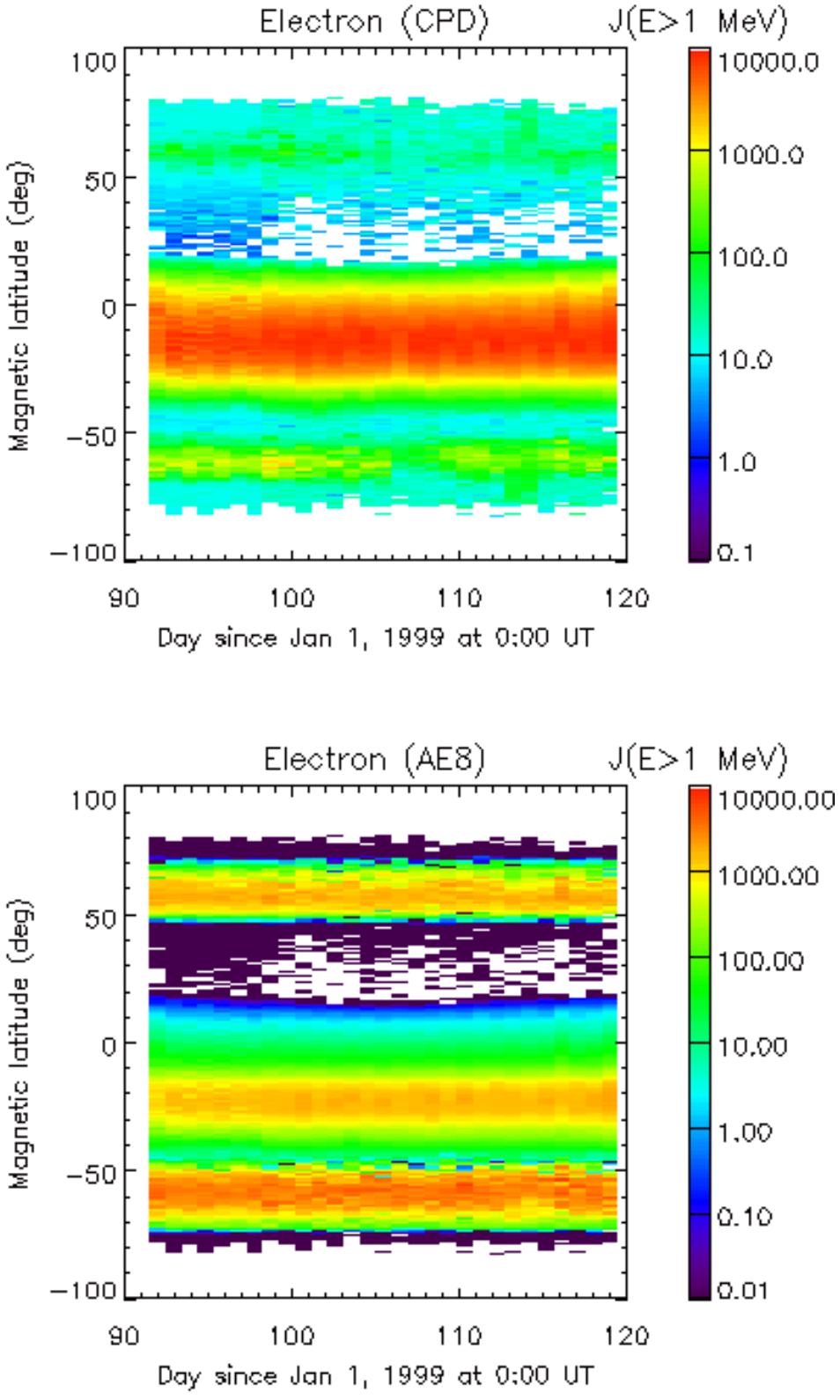

Figure 4.15: Maps of high energy electron flux as a function of time and magnetic latitude. There is an important difference between the SAA peak of electron flux predicted by AE8-MAX and that detected by the CPD.

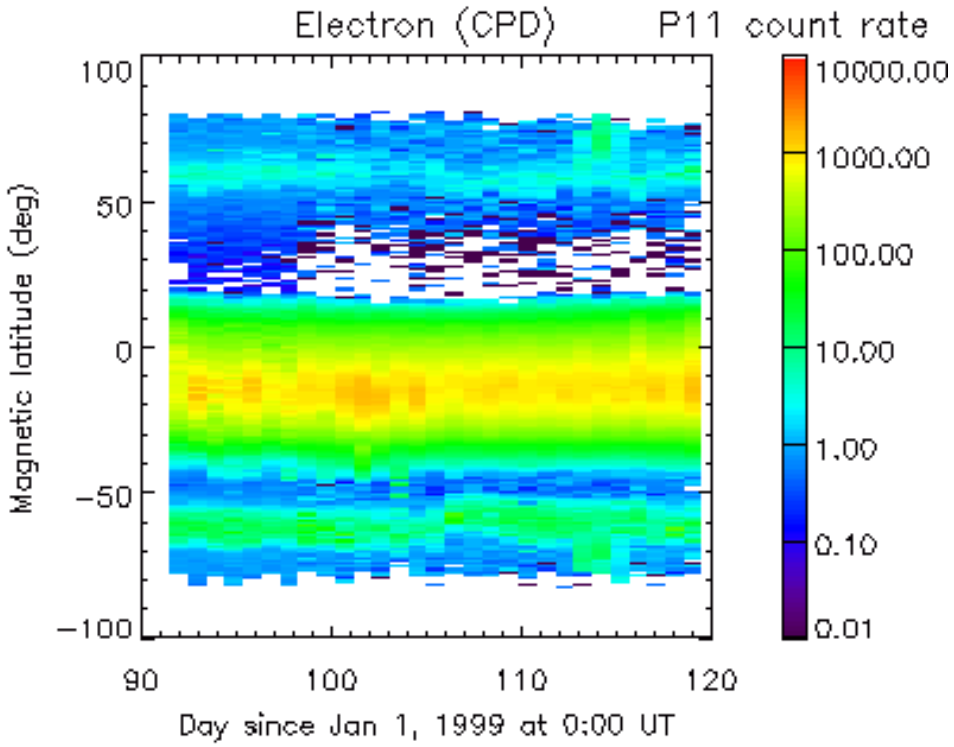

Figure 4.16: Counting rates in the P11 channel that counts efficiently electrons with $E > 0.02\ MeV$.

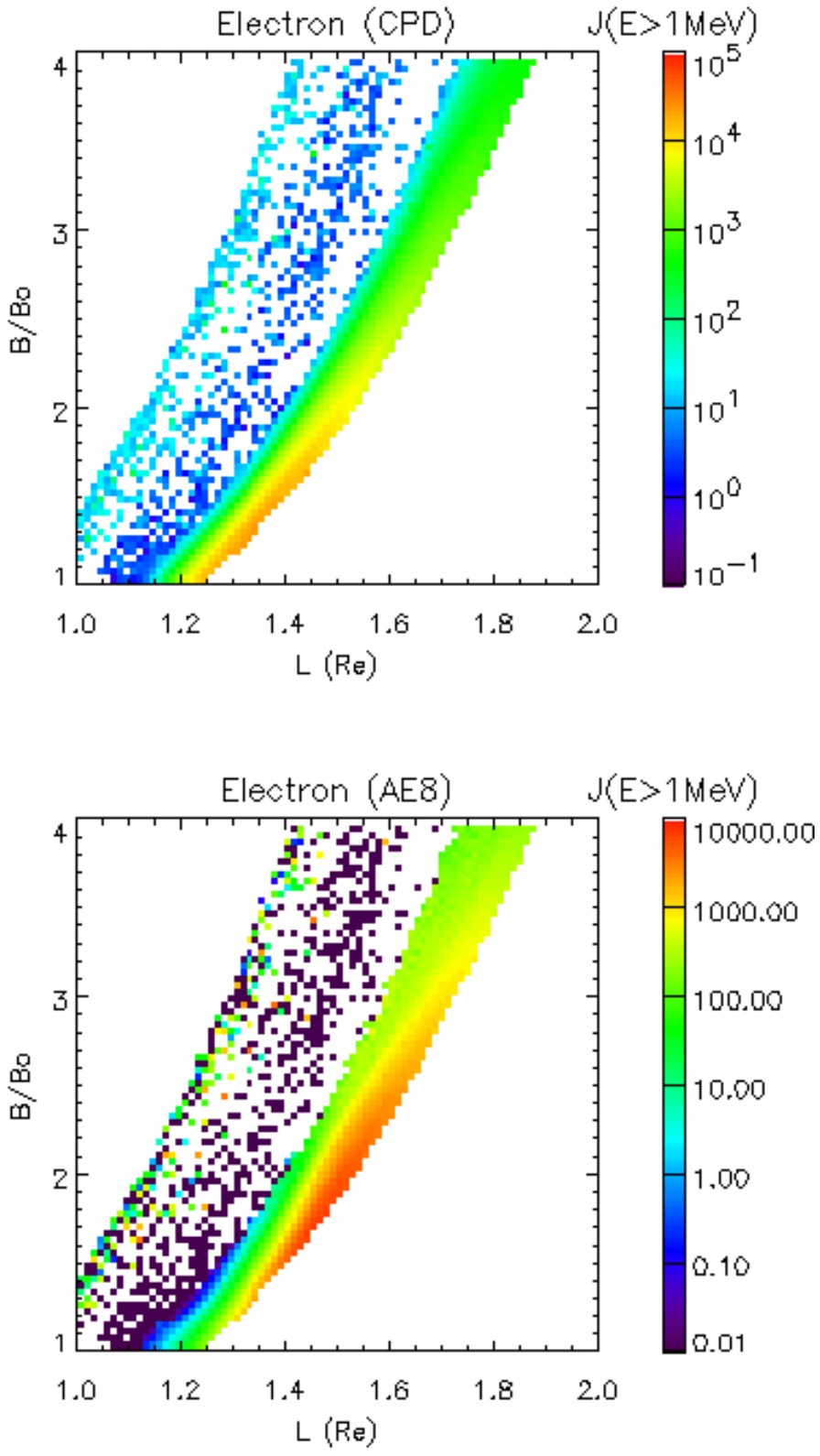

Figure 4.17: $(B/B_0, L)$ *maps of high energy electron flux.*

Chapter 5

Conclusion

The study presented in this report was initiated mainly to model the charged particle fluxes encountered along the ØRSTED orbit. By dedicating the needed time and tools to the detector characterization, we succeeded in extracting the fluxes of protons and electrons from the CPD raw data.

- *The flux of high energy protons is an order of magnitude higher than the prediction of AP8-MAX. The CPD proton fluxes remain higher than the NASA AP-8 MAX model predictions, even when the observed counting rates are supposed to come from a 4π solid angle. This NASA model is used in CREME when protons LET are to be taken into account for SEU rate calculations. Therefore, SEU rates may be underestimated by CREME for LEO satellites.*
- *The proton fluxes deduced from the CPD raw data are a factor 2 higher than the SAMPEX/PSB97 predictions.*
- *The CPD is the only energetic particle detector on board the ØRESTED satellite. The proton fluxes resulting from the CPD data need to be checked against results from other detectors accomodated to satellites having a similar orbit. This would help to determine whether a part of the CPD observed counting rates resulted from protons impacting the sensor from the satellite back side or not.*
- *The uncertainty on the proton fluxes amounts to ≈30%.*
- *The actual location of high energy electrons detected by the CPD is found to be more extended and shifted towards the north as compared to the results of the NASA AE8-MAX model.*

More data from other satellites and instruments are needed in order to check the results of this study. In particular, the consequences of proton flux underestimation by the CREME software should be evaluated in order to improve it as a tool to predict damages in electronic components on board satellites.

Bibliography

[1] D. Heynderickx and J. Lemaire, Coordinate systems for mapping low-altitude trapped particle fluxes, AERONOMICA ACTA A, No. 389, 1995.

[2] M. Cyamukungu, Gh. Grégoire, J. Lemaire and P. Stauning, The Charged Particle Detector (CPD) on the ØRSTED satellite: description and evaluation, Technical Report A, Louvain-la-Neuve, September 1997.

[3] P. Stauning, P. Davidsen and M. Cyamukungu, Detection of radiation-induced anomalies in the memory circuits of the ØRSTED satellite, (submitted to Adv. Space Res.).

[4] M. Cyamukungu, Gh. Grégoire, P. Stauning, and J. Lemaire, The Charged Particle Detector (CPD): Data Analysis Methodology, Proceedings of the ØRSTED 3rd International Science Team Meeting, Grasse, France, May 2-4, 2000.

[5] J.D. Sullivan, Geometrical factor and directional response of single and multi-element particle telescopes, Nuclear Instruments and Methods, 95 (1971) 5 - 11.

[6] M. Cyamukungu, Gh. Grégoire, D. Heynderickx, M. Kruglanski, J. Lemaire, J.B. Blake and R.S. Selesnick, Proton spectra detected by the Proton Switches on the CRRES satellite, Journal of Spacecraft and Rockets, Vol. 38(4) (2001) 584-589).

List of Figures

List of Tables